Identification of hydrated silicate minerals on Mars using MRO-CRISM: Geologic context near Nili Fossae and implications for aqueous alteration

Bethany L. Ehlmann,[1] John F. Mustard,[1] Gregg A. Swayze,[2] Roger N. Clark,[2] Janice L. Bishop,[3,4] Francois Poulet,[5] David J. Des Marais,[4] Leah H. Roach,[1] Ralph E. Milliken,[6] James J. Wray,[7] Olivier Barnouin-Jha,[8] and Scott L. Murchie[8]

Received 23 January 2009; revised 8 May 2009; accepted 11 June 2009; published 23 October 2009.

[1] The Noachian terrain west of the Isidis basin hosts a diverse collection of alteration minerals in rocks comprising varied geomorphic units within a 100,000 km^2 region in and near the Nili Fossae. Prior investigations in this region by the Observatoire pour l'Minéralogie, l'Eau, les Glaces, et l'Activité (OMEGA) instrument on Mars Express revealed large exposures of both mafic minerals and iron magnesium phyllosilicates in stratigraphic context. Expanding on the discoveries of OMEGA, the Compact Reconnaissance Imaging Spectrometer for Mars (CRISM) aboard the Mars Reconnaissance Orbiter (MRO) has found more spatially widespread and mineralogically diverse alteration minerals than previously realized, which represent multiple aqueous environments. Using CRISM near-infrared spectral data, we detail the basis for identification of iron and magnesium smectites (including both nontronite and more Mg-rich varieties), chlorite, prehnite, serpentine, kaolinite, potassium mica (illite or muscovite), hydrated (opaline) silica, the sodium zeolite analcime, and magnesium carbonate. The detection of serpentine and analcime on Mars is reported here for the first time. We detail the geomorphic context of these minerals using data from high-resolution imagers onboard MRO in conjunction with CRISM. We find that the distribution of alteration minerals is not homogeneous; rather, they occur in provinces with distinctive assemblages of alteration minerals. Key findings are (1) a distinctive stratigraphy, in and around the Nili Fossae, of kaolinite and magnesium carbonate in bedrock units always overlying Fe/Mg smectites and (2) evidence for mineral phases and assemblages indicative of low-grade metamorphic or hydrothermal aqueous alteration in cratered terrains. The alteration minerals around the Nili Fossae are more typical of those resulting from neutral to alkaline conditions rather than acidic conditions, which appear to have dominated much of Mars. Moreover, the mineralogic diversity and geologic context of alteration minerals found in the region around the Nili Fossae indicates several episodes of aqueous activity in multiple distinct environments.

Citation: Ehlmann, B. L., et al. (2009), Identification of hydrated silicate minerals on Mars using MRO-CRISM: Geologic context near Nili Fossae and implications for aqueous alteration, *J. Geophys. Res.*, *114*, E00D08, doi:10.1029/2009JE003339.

1. Introduction

[2] Landed measurements by the Mars Exploration Rovers (MER) and orbital visible and near-infrared data from the Observatoire pour l'Minéralogie, l'Eau, les Glaces, et l'Activité (OMEGA) and the Compact Reconnaissance Imaging Spectrometer for Mars (CRISM) have revealed a rich mineralogic record of aqueous alteration on Mars that complements preexisting geomorphic data recording the past presence of liquid water [*Squyres et al.*, 2004; *Bibring et al.*, 2005; *Murchie et al.*, 2009a]. Sulfate minerals found in northern circumpolar deposits, Vallis Marineris, the plains of Terra Meridiani, and soils around Columbia Hills in Gusev crater probably indicate precipitation of salts from

[1]Department of Geological Sciences, Brown University, Providence, Rhode Island, USA.
[2]U.S. Geological Survey, Denver, Colorado, USA.
[3]SETI Institute, Mountain View, California, USA.
[4]NASA Ames Research Center, Mountain View, California, USA.
[5]Institut d'Astrophysique Spatiale, Université Paris Sud, CNRS, Orsay, France.
[6]Jet Propulsion Laboratory, California Institute of Technology, Pasadena, California, USA.
[7]Department of Astronomy, Cornell University, Ithaca, New York, USA.
[8]Johns Hopkins University Applied Physics Laboratory, Laurel, Maryland, USA.

0148-0227/09/2009JE003339

acidic surface and near surface waters in the Hesperian epoch [*Gendrin et al.*, 2005; *Bibring et al.*, 2006; *Squyres et al.*, 2004; *Arvidson et al.*, 2006; *Haskin et al.*, 2005]. During the earlier Noachian epoch on the other hand, a different process of longer-lived water-rock interaction at neutral to alkaline pH is indicated by the presence of phyllosilicate minerals, mostly iron magnesium smectite clays [*Bibring et al.*, 2006; *Chevrier et al.*, 2007]. OMEGA revealed large phyllosilicate exposures in the well-exposed Noachian terrains around Mawrth Vallis and Nili Fossae as well as in scattered outcrops in the southern highlands [*Poulet et al.*, 2005]. Subsequent investigations at smaller spatial scales by CRISM reveal that phyllosilicates are a relatively common feature of the southern highlands occurring, apparently without geographic restrictions, in association with hundreds of impact craters [*Mustard et al.*, 2008]. Additionally, CRISM data have allowed discovery of the diversity of hydrated minerals present. In addition to previously detected smectites and chlorite [*Poulet et al.*, 2005], CRISM near-infrared (NIR) spectral data have been used to identify kaolinite, potassium micas such as illite or muscovite, hydrated silica, magnesium carbonate, and prehnite [*Mustard et al.*, 2008; *Milliken et al.*, 2008; *Ehlmann et al.*, 2008a; D. Buczkowski et al., manuscript in preparation, 2009]. Along with the detections of zeolite and serpentine reported in this study, these minerals indicate that a variety of aqueous alteration processes were probably at work on Noachian Mars to generate such mineralogic diversity.

[3] The Noachian epoch spans the period from the first appearance of a solid crust to approximately 3.6 Ga [*Hartmann and Neukum*, 2001], and the environment(s) in which aqueous alteration occurred are not yet well defined. In comparison to the precipitation of salts from solution, phyllosilicates require a more extended period of time to form, either from topotactic alteration of mafic mineral grains or by neoformation from solution [*Eberl*, 1984]. Common terrestrial processes for phyllosilicate formation include leaching and pedogenic alteration, subaqueous alteration in basins, precipitation in hydrothermal systems, and metamorphism and diagenesis. Mineral assemblage, alteration mineral abundance, and stratigraphic setting are constraints that are at least partially ascertainable from orbit and that allow distinguishing among phyllosilicate formation mechanisms.

[4] On Mars, alteration of parent materials to phyllosilicates may have been associated with precipitation, runoff and soil formation as in the modern terrestrial hydrological cycle. Indeed, the Mawrth Vallis region shows well-developed stratigraphy of Al phyllosilicates overlying Fe/Mg smectites [*Wray et al.*, 2008; *Bishop et al.*, 2008a; *McKeown et al.*, 2009; E. Z. Noe Dobrea et al., Clay bearing units in the region around Mawrth Vallis: Stratigraphy, extent, and geologic origin, submitted to *Journal of Geophysical Research*, 2009] such as might be expected to be produced by a top-down leaching process. However, elsewhere, source regions for valley networks are not especially enhanced in phyllosilicate minerals [*Bibring et al.*, 2006], and phyllosilicates associated with fluvial lacustrine deposits discovered so far are most likely transported, not precipitated in situ [e.g., *Mustard et al.*, 2008; *Grant et al.*, 2008; *Ehlmann et al.*, 2008b]. An alternative hypothesis to surface formation of phyllosilicates by weathering is that the formation of phyllosilicates occurred primarily in the subsurface, possibly driven by hydrothermally mediated crustal cooling [e.g., *Parmentier et al.*, 2008]. The intense meteoric bombardment of early Mars may also have played a role in phyllosilicate formation, perhaps in serving as a heat source generating liquid water from a cryosphere [e.g., *Newsom*, 1980]; impact craters on Earth commonly host hydrothermal deposits with phyllosilicates [*Allen et al.*, 1982; *Naumov*, 2005; *Nelson et al.*, 2005]. Key questions for addressing the timing, nature, and extent of aqueous alteration include: Which phyllosilicates are present? What other altered and unaltered minerals are present? What is the geomorphic setting and distribution of these diverse phases? And, how much phyllosilicate is present?

[5] The question of abundance is difficult to address owing to multiple scattering of photons in the visible and near-infrared wavelengths leading to nonlinearities in the relative contributions of components in mixtures, although initial efforts with OMEGA data have begun to address this question [*Poulet et al.*, 2008]. This paper focuses on the methodology for identification of diverse hydrated silicates, along with associated silicate hydroxides and carbonates, and mapping of their occurrences using CRISM NIR data. With the exception of the aluminum smectite montmorillonite, all nonsulfate hydrated minerals detected to date from orbit can be found in the region west of the Isidis basin, in and around the Nili Fossae. The remarkable mineralogic diversity of this region is probably due to a combination of factors: (1) a geologic history involving apparently multiple instances of alteration by liquid water, (2) the availability of starting materials of distinct mafic compositions, and (3) the action of erosion in producing excellent bedrock exposures.

[6] After briefly reviewing the history and geologic setting of the study area west of Isidis (section 2) and methods of data analysis (section 3), we detail in section 4 the spectral data used as the basis for the detection of each hydrated mineral phase: Fe and Mg smectites, chlorite, prehnite, serpentine, kaolinite, K mica, the Na zeolite analcime, hydrated silica, and carbonate. We then describe in section 5 the distribution and geomorphic setting of the mineral phases found in the region around the Nili Fossae. By studying the geologic setting and associations of minerals, the nature of the formation environment can be partially constrained. We discuss the aqueous environments indicated, constraints on timing, and key outstanding questions from our study in section 6. A companion paper provides an updated, comprehensive geologic history of the circum-Isidis region, examining the detailed stratigraphy of various mineral-bearing units, including mafic minerals [*Mustard et al.*, 2009]. We focus here specifically on the identification of alteration minerals and on the various environments of aqueous alteration that can be ascertained, including evidence for low-temperature metamorphic or hydrothermal alteration in the subsurface.

2. Geologic Setting and Study Area

[7] West of the 1900 km Isidis basin, the cratered, Noachian-aged crust is cut by a series of concentric frac-

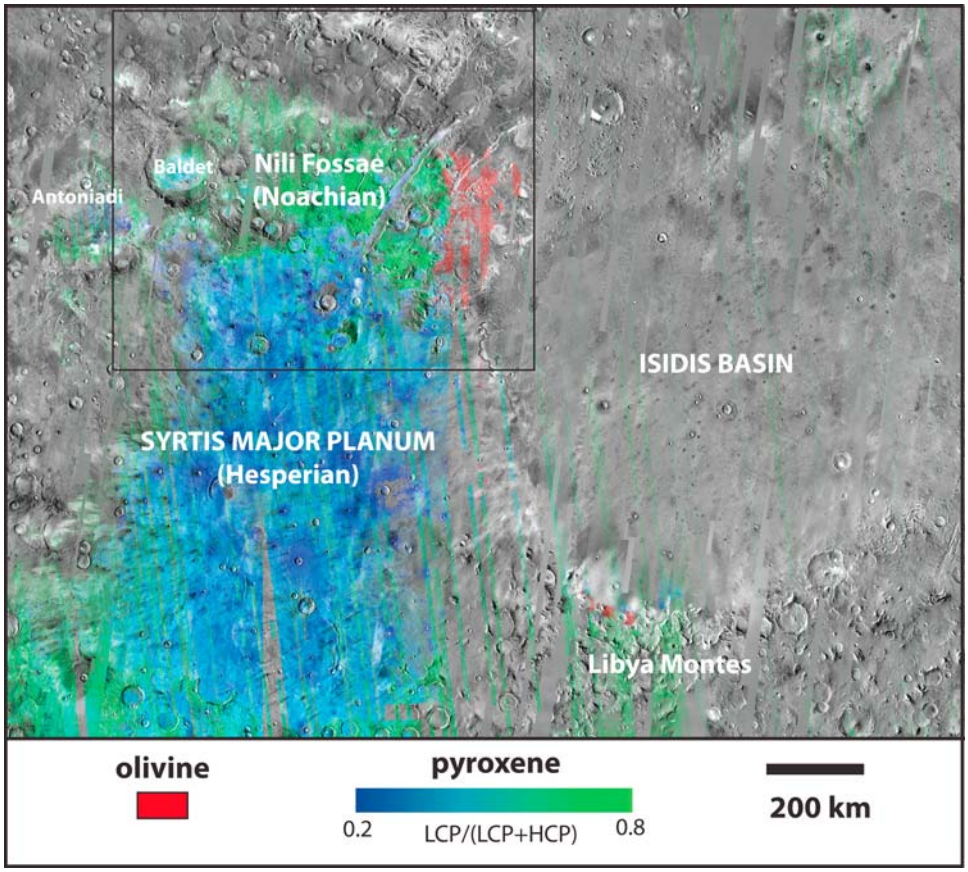

Figure 1. Thermal Emission Imaging System (THEMIS) daytime infrared mosaic with mafic mineralogic parameters overlain. In pyroxene-bearing terrains, the ratio of low-calcium pyroxene to total (low calcium and high calcium) pyroxene is mapped with CRISM and OMEGA data using the modified Guassian model [mapping by P. Thollot according to the methods in the work of *Mustard et al.*, 2005] so that terrains enriched in low-calcium pyroxene are green and those enriched in high-calcium pyroxene are blue. The presence of olivine is indicated in red and mapped with OMEGA data using the olivine parameter [*Pelkey et al.*, 2007].

tures formed by normal faulting in response to structural readjustment that shortly followed the Isidis impact around ~3.9 Ga (Figures 1 and 2) [*Wichman and Schultz*, 1989; *Greeley and Guest*, 1987; *Werner*, 2005]. These downdrop graben, collectively referred to as the Nili Fossae, extend from 20°N to 26°N, are up to 600 m deep and, along with the surrounding terrain, have been heavily modified by erosion and infilling. To the south, younger volcanic lavas from Syrtis Major overlie the Noachian terrain and partially fill some of the fossae [*Greeley and Guest*, 1987]. The contact between the Hesperian Syrtis Major lavas and the Noachian etched plains marks a distinct compositional boundary between two crustal units (Figure 1). Generally the Syrtis Major lavas are enriched in high-calcium pyroxene, while low-calcium pyroxene-bearing materials are more common in the Noachian cratered terrains [*Mustard et al.*, 2005]. The eastern portion of the Nili Fossae region also is the largest exposed olivine-bearing region on the planet [*Hamilton et al.*, 2003; *Hoefen et al.*, 2003; *Hamilton and Christensen*, 2005; *Mustard et al.*, 2005]. Although much of the olivine is in the form of sand, the olivine-bearing bedrock from which it is sourced is a contiguous unit that crops out over hundreds of square kilometers [*Hamilton and Christensen*, 2005; *Mustard et al.*, 2009]. This bedrock unit likely originated from materials ejected during the Isidis impact [*Mustard et al.*, 2007, 2009] or, alternatively, may represent low-viscosity lava flows [*Hamilton and Christensen*, 2005; *Tornabene et al.*, 2008].

[8] Our study area encompasses the Noachian cratered terrain east from Nili Fossae westward to the eastern margin of the Antoniadi basin and from the northern Nilo-Syrtis chaos southward to craters on the northern margin of the Hesperian Syrtis Major formation (Figures 2 and 3). Both the Hesperian and Noachian units have sapping channels, fluvial valleys, and depositional fans that provide geomorphic evidence for sustained surface water flow [*Mangold et al.*, 2007]. The largest such system is the watershed of Jezero crater, which drained 15,000 km^2 during the late Noachian or early Hesperian to form a paleolake with deltaic deposits [*Fassett and Head*, 2005; *Ehlmann et al.*, 2008b]. However, while the Noachian terrain shows extensive mineralogic evidence of aqueous alteration, discussed

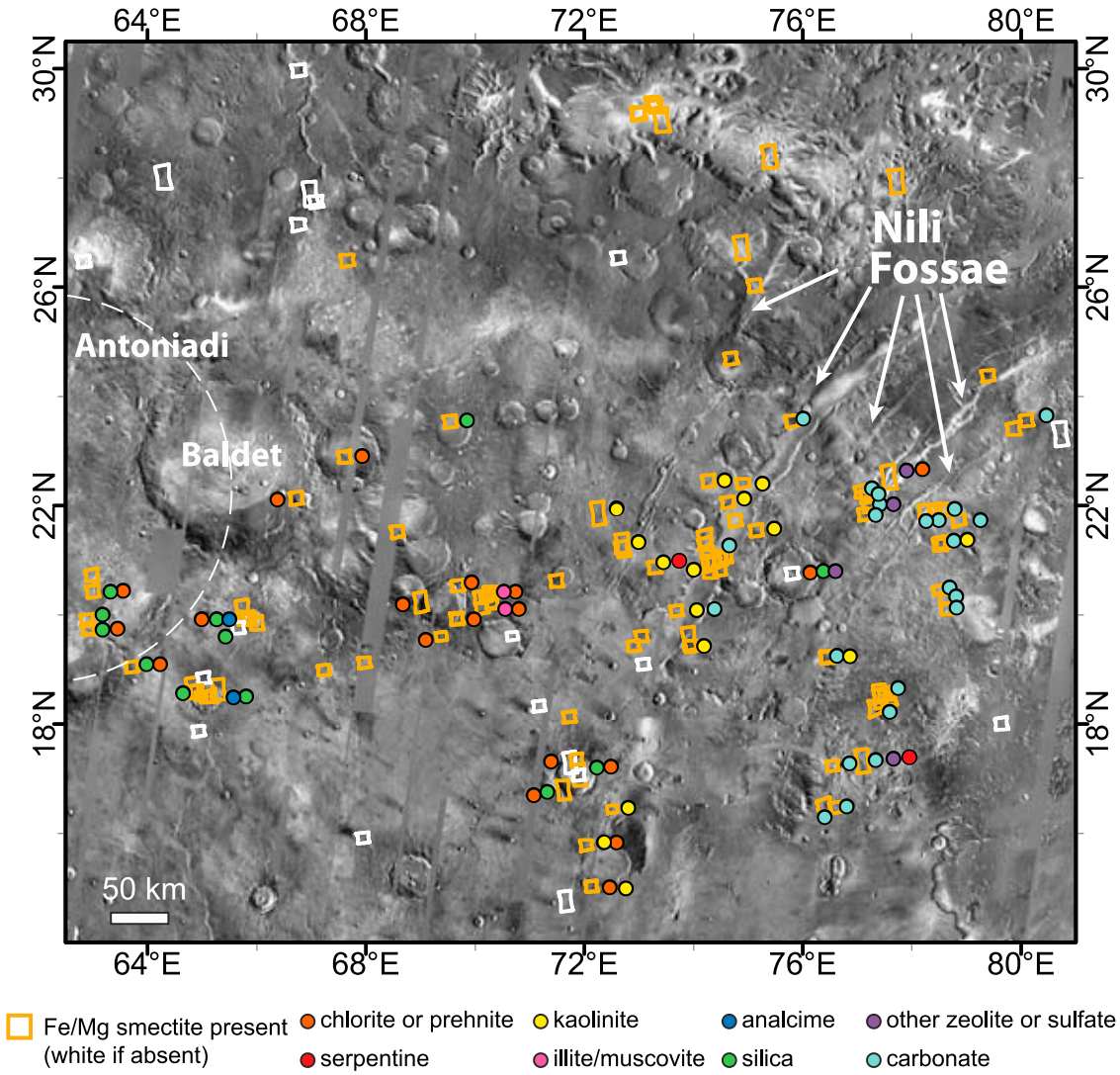

Figure 2. THEMIS daytime infrared mosaic of the study region west of Isidis indicating locations of hydrated minerals. Outlines of CRISM targeted images through 31 August 2008 (2008_244) are indicated by white outlines if no phyllosilicates are present and orange if Fe/Mg smectite is present in the observation. Presence of other hydrated minerals within the observation is indicated by the colored circles located next to the CRISM observation. Where observations have significant overlap, symbols indicating mineral presence are only shown once for the collection of observations.

further in this paper, the Hesperian Syrtis Major lavas do not show evidence in orbital data of hydrated minerals [*Mangold et al.*, 2007].

3. Data Sets and Methods

3.1. Data Processing and Selection of Spectra

[9] CRISM is a hyperspectral imaging spectrometer on the Mars Reconnaissance Orbiter (MRO) with 544 channels that sample the visible to near-infrared spectral region from 0.4 to 4.0 μm using two detectors [*Murchie et al.*, 2007a]. The S detector samples wavelengths 0.4–1.0 μm, and the L detector samples wavelengths 1.0–4.0 μm. CRISM operates in two modes: (1) a 72-channel mapping mode that will provide global coverage at 200 m/pixel and (2) a full 544-channel targeted mode that provides 10 $\times$ 10–20 km images at a resolution of 15–38 m/pixel. Results from the L detector data of the latter, high-resolution mode are the focus of this paper and allow mapping of mafic minerals and hydrated or hydroxylated alteration minerals.

[10] Spacecraft data were converted to I/F as described by *Murchie et al.* [2007a, 2009b]. Prior to spectral analysis, simple atmospheric and photometric corrections were applied to CRISM data cubes to correct for viewing geometry and separate out the contribution of reflected light from the surface from that of the atmosphere. Cubes were photometrically corrected by dividing by the cosine of the incidence angle, assuming that to first order the surface behaves as a Lambertian scatterer. The contribution of the atmosphere was removed using the volcano scan correction method, also successfully employed by the OMEGA mission [*Mustard et al.*, 2005]. In the volcano scan method, an atmospheric transmission spectrum is derived from observations at the base and top of Olympus Mons. For a given

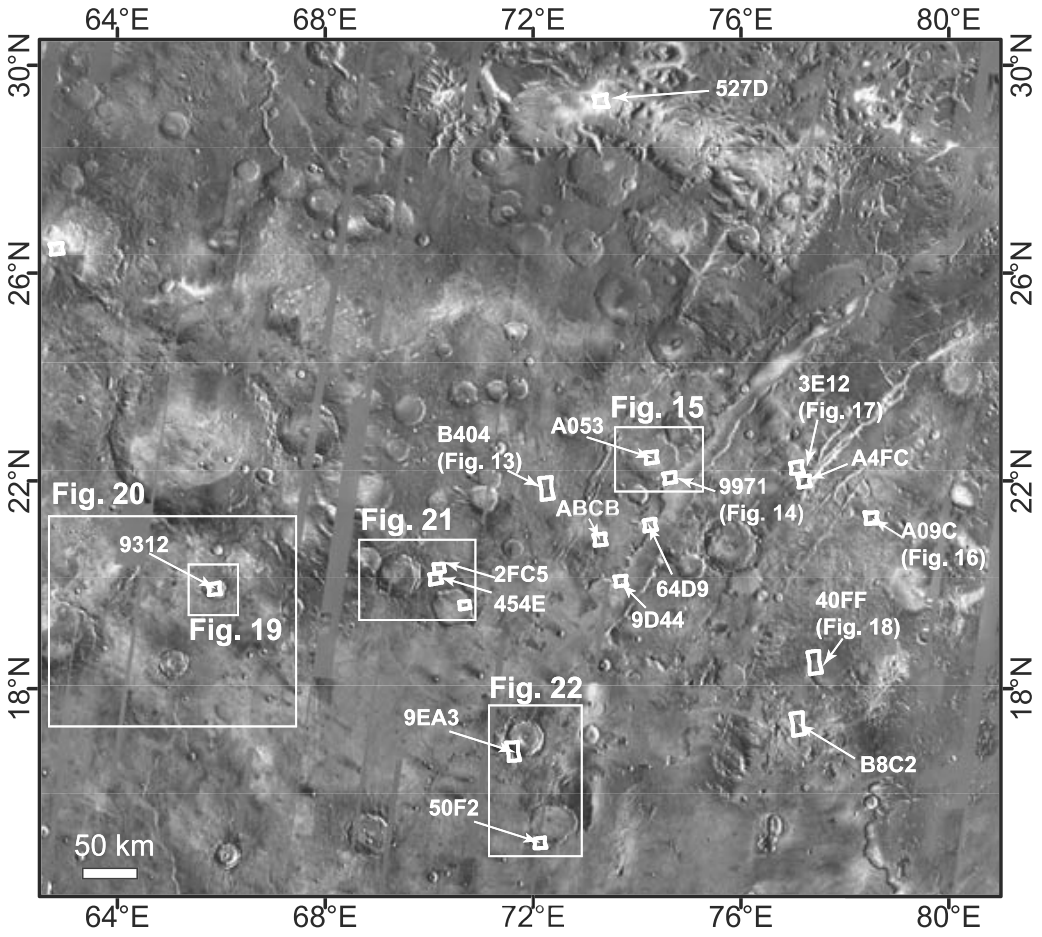

Figure 3. THEMIS daytime infrared mosaic of the study region west of Isidis indicating four-character hexadecimal IDs for images and spectra specifically referred to in this paper. Outlines of Figures 13–22 are also shown.

CRISM observation the atmospheric transmission spectrum is scaled to match the band depth of the 2-μm CO_2 feature in each pixel, and then the observed spectrum is divided by this scaled spectrum. The technique, which assumes a multiplicative atmospheric contribution to surface spectra, removes absorption features resulting from atmospheric gases with few residual artifacts, but aerosols and ices are not accounted for and may lead to spectral slopes or residual absorptions. Overall, the volcano scan technique is simple and efficient for correcting large numbers of CRISM scenes. Results compare favorably with the more rigorous, but time-intensive scene-specific radiative transfer modeling employed using DISORT [*Arvidson et al.*, 2006] provided that aerosol abundances at the time of imaging are not appreciably different from those present at the time of the volcano scan observation. Nevertheless, small positive features or residual absorptions near 2 μm are still commonly present even in atmospherically corrected CRISM data (as is apparent in some CRISM spectra from Figures 4–12). These are artifacts of the atmospheric calibration methods rather than features of use in mineral identification.

[11] Following atmospheric correction, a noise removal algorithm that removes data spikes in both the spectral and spatial domains but does not affect broader absorptions of mineralogic interest was implemented [*Parente*, 2008]. In addition, to highlight spectral differences between areas and reduce residual atmospheric and instrumental artifacts in spectra, average spectra from regions of interest were divided by spectra from a dusty or spectrally unremarkable region in the same scene. When possible, an $n \times n$ pixel spectrum of similar albedo to the $n \times n$ pixel spectrum of interest and from the same column of the unprojected image was used as the denominator. Sampling in the same column reduces detector-dependent noise. Alternatively, larger, more irregularly shaped regions of interest for the numerator and denominator were identified, not necessarily from the same column. In both cases, tens to thousands of pixels were averaged to minimize spurious absorptions due to noise (Table A1). Even with these steps, some artifacts persist. After removing CRISM known bad spectral channels, some known residual artifacts are common near 2.0 μm owing to errors in atmospheric calibration and at 1.65 μm owing to a detector filter boundary [*Murchie et al.*, 2009b]. Single channel spikes in spectra that are too narrow for absorptions related to mineralogy are also removed or ignored. Spectra used in the detailed analysis of section 4 are either from the central portion of the scene or have been corrected for column-dependent wavelength shifts due to the CRISM spectral smile by using the CDR WA file [*Murchie et al.*, 2007a, 2007b]. Band centers reported here

from the CRISM data have an error of approximately ±0.01 μm, the average spectral sampling interval of the instrument.

3.2. Mineral Identification and Mapping

[12] Hydrated silicate minerals are identified in CRISM spectroscopic data by overtones and combinations of fundamental vibrational absorption features in the region from 1.0 to 2.6 μm. The presence of H_2O in the mineral structure is expressed near 1.9 μm by a combination tone of the fundamental bending and stretching vibrations of the water molecule. Overtones of structural OH stretching vibrations occur near 1.4 μm, as do combination tones of the H_2O molecule [*Bishop et al.*, 1994]. The position of the OH overtone shifts depending on the type of octahedral cation (Mg, Al, Fe) from 1.38 to 1.43 μm for many phyllosilicates [e.g., *Bishop et al.*, 2002a, 2002b]. From 2.1 to 2.5 μm, additional structural OH combination stretching plus bending vibrations are found, and their precise wavelength position depends on the type of octahedral cation and mineral structure. For example, Fe-OH absorptions in smectites are found near 2.28 μm whereas Al-OH absorptions are found near 2.20 μm [*Clark et al.*, 1990a]. Overtones/combinations of fundamental vibrations related to H_2O in zeolites [*Cloutis et al.*, 2002] and CO_3 in carbonates [*Gaffey*, 1987] are also found in the 2–2.6 μm wavelength region.

[13] These absorptions can be parameterized and mapped spatially, e.g., by calculating absorption band depth for each pixel in an image. Here, we utilize the standard parameter set of *Pelkey et al.* [2007] formulated for multispectral CRISM images along with custom parameters for absorptions at 1.9, 2.2, and 2.5 μm. A 1.9-μm absorption occurs in minerals with H_2O, a 2.2-μm absorption occurs in minerals such as Al phyllosilicates and opaline silica with Al-OH and Si-OH bonds, and a 2.5-μm absorption occurs minerals such as in carbonates and zeolites. The devised custom parameters take advantage of the additional bands available in hyperspectral targeted images to average out noise and reduce spurious high values or, in the case of BD2500, provide additional parameters to the standard multispectral CRISM set and are formulated as follows:

$$\mathrm{BD1900H} = 1 - \mathrm{AVG}(\mathrm{R1908} : \mathrm{R1914})/(\mathrm{AVG}(\mathrm{R1862} : \mathrm{R1875}) + \mathrm{AVG}(\mathrm{R2112} : \mathrm{R2126}))$$

$$\mathrm{BD2200} = 1 - 2{*}\mathrm{AVG}(\mathrm{R2199}, \mathrm{R2205})/(\mathrm{AVG}(\mathrm{R2132}, \mathrm{R2146}) + \mathrm{AVG}(\mathrm{R2252}, \mathrm{R2258})$$

$$\mathrm{BD2500} = 1 - \mathrm{AVG}(\mathrm{R2500}, \mathrm{R2510})/\mathrm{AVG}(\mathrm{R2380}, \mathrm{R2540})$$

where, for example, R1980 is the reflectance at 1.980 μm, and avg(R1908:R1914) is the average reflectance over all wavelengths between 1.908 and 1.914 μm. The other commonly employed parameters from the standard *Pelkey et al.* [2007] set were D2300, used for mapping absorption bands near 2.3 μm (common in Fe/Mg smectites and carbonates), and BD2350 used for mapping specifically the 2.35-μm absorption band (common in chlorites, prehnite, illite/muscovite, and some carbonates). Generally, threshold values used in mapping are 0 to 0.05. However, factors other than absorption band strength from minerals of interest can affect parameter values computed, e.g., detector noise, aerosols, continuum slope; so threshold values were manually adjusted on an image-by-image basis by analyzing the spectral data to verify that parameter maps were indeed mapping out occurrences of spectra corresponding to definitive mineral identifications. Actual lower bounds used ranged from −0.005 to 0.01 and upper bounds from 0.02 to 0.1. Computed CRISM image data and parameter maps were then map projected using the line of sight intercept of each detector element with the 128-pixel per degree MOLA shape model of Mars contained in band 10 of the Derived Data Record (DDR) accompanying each image [*Murchie et al.*, 2007b, 2009b].

[14] In order to understand the geomorphology and geologic setting of the mineral detections, these CRISM parameter maps were coregistered with and combined with a variety of imaging data sets. These include coordinated observations acquired by the two high-resolution MRO cameras, the Context Imager (CTX) and the High Resolution Science Experiment (HiRISE) cameras on MRO, which acquire images at 5 m/pixel and 0.25 m/pixel, respectively [*Malin et al.*, 2007; *McEwen et al.*, 2007]. Additionally, Thermal Emission Imaging System (THEMIS) day infrared images at 100 m/pixel were sometimes employed [*Christensen et al.*, 2004]. Mars Orbiter Laser Altimeter elevation data were used to view three-dimensional representations of the topography. These data were obtained for individual images from their DDRs and from the 128 pixel per degree global map for regional topographic information.

[15] Full- and half-resolution CRISM images were targeted to follow up on detections of altered and unaltered minerals using coarser spatial resolution OMEGA and CRISM mapping data, to focus on areas where prior data sets indicated exposed stratrigraphy or interesting morphologic features, and as ride-alongs to HiRISE and CTX imaging requests. Placement of CRISM targeted images reflects an attempt to ascertain geologic relationships between mineralogic units exposed from beneath dust and capping materials with no distinctive NIR spectral signature rather than a systematic survey of the study area.

4. Identified Minerals

[16] Most of the numerous diverse hydrated silicate minerals recently identified on Mars by CRISM can be found in the region around Nili Fossae [*Mustard et al.*, 2008]. On the basis of CRISM VNIR spectra, below we detail the rationale for the identification of multiple varieties of Fe/Mg smectite, chlorite, prehnite, serpentine, kaolinite, a K mica such as illite or muscovite, hydrated silica, the zeolite analcime, and magnesium carbonate. We also describe spectra consistent with either a mixture of silica and Mg sulfate or silica and zeolite. Locations of CRISM observations from which spectra were derived are shown in Figure 3. Tables A1 and A2 provide the locations and number of pixels averaged for all CRISM spectra as well as complete identifying information for library spectra used in Figures 4–12. The intent of section 4 is to detail the basis

for these phases' unique identification so that they may be replicated by future users of CRISM data and also to provide detailed discussions of mineral phases and uncertainties of interest for geochemical modeling. The discussion of the geologic context of these minerals begins in section 5. Three guiding principles used in our mineral identifications were that (1) absorption features in the CRISM spectra should be consistent with the same features in laboratory spectra of the mineral, (2) these features should not be consistent with those of other minerals (for uniqueness), and (3) no strong absorptions should be left unexplained.

4.1. Fe/Mg Smectites

[17] As previously revealed by the OMEGA spectrometer, iron magnesium smectites are the areally dominant phyllosilicate in the Nili Fossae region [*Poulet et al.*, 2005; *Mangold et al.*, 2007]. Fe/Mg smectites are 2:1 phyllosilicates and form from weathering and hydrothermal processes. They are identified in spectroscopic data by a characteristic vibrational absorption near 2.3 μm and a 1.9-μm band indicating molecular H_2O (Figure 4). A 1.4-μm band is commonly discernible as are additional combination tones near 2.4 μm. CRISM targeted observations reveal a suite of spectra with these characteristic features in the Nili Fossae region but which show considerable variation both within and between scenes. A subset of the diverse spectra we classify as Fe/Mg smectites is shown in Figure 4. We focus here on determining with greater precision the likely chemistry of the various Fe/Mg smectites in Nili Fossae.

[18] A variety of smectite compositions are possible depending on Al, Fe, and Mg occupancy of the octahedral sheet and substitution of cations in the interlayer to balance the charge. Smectites have a general formula of M^{+}_{x-y+2z} (R^{2+}_{3-y-z}, R^{3+}_{y}, $\square_z$) $Si_{4-x}Al_xO_{10}(OH)_2$ where $0.3 \leq x-y+2z \leq 0.6$ and z refers to the number of vacancies per unit cell in the octahedral layer [*Meunier*, 2005]. There is continuous solution between Fe and Mg smectite end-members [*Grauby et al.*, 1994], and compositional variation is expressed in variations in the NIR spectra. In particular, the relative proportions of Fe, Mg, and Al cations in the octahedral site dictate the presence and position of bands from 1.35 to 1.45 μm and from 2.0 to 2.5 μm. That the smectites in Nili Fossae are predominantly Fe/Mg rather than Al is determined by the presence of an absorption near 2.3 μm rather than near 2.2 μm. The 2.3-μm band results from combination tones of the 2Fe-OH and 3Mg-OH bends and stretches, and a more subtle band at 2.4 μm is also related to these bonds [*Clark et al.*, 1990a; *Frost et al.*, 2002; *Bishop et al.*, 2002b]. The precise position of the 2.3-μm band varies depending on the relative proportions of Fe versus Mg. For example, dioctahedral nontronite, the Fe end-member, has a band center near 2.29 μm [*Grauby et al.*, 1994; *Bishop et al.*, 2002b; *Frost et al.*, 2002], whereas the trioctahedral Mg end-members saponite and hectorite have absorptions near 2.31–2.32 μm (Figure 4b) [*Clark et al.*, 1990a]. Aluminum, if present in smectite, is indicated by a strong 2.21 μm 2Al-OH combination tone or a somewhat weaker Al,Fe-OH combination tone at 2.23–2.25 μm [*Bishop et al.*, 2002a, 2008b].

[19] In the Nili Fossae region, the 2.3-μm band varies in shape and strength from a sharp absorption of up to 10%

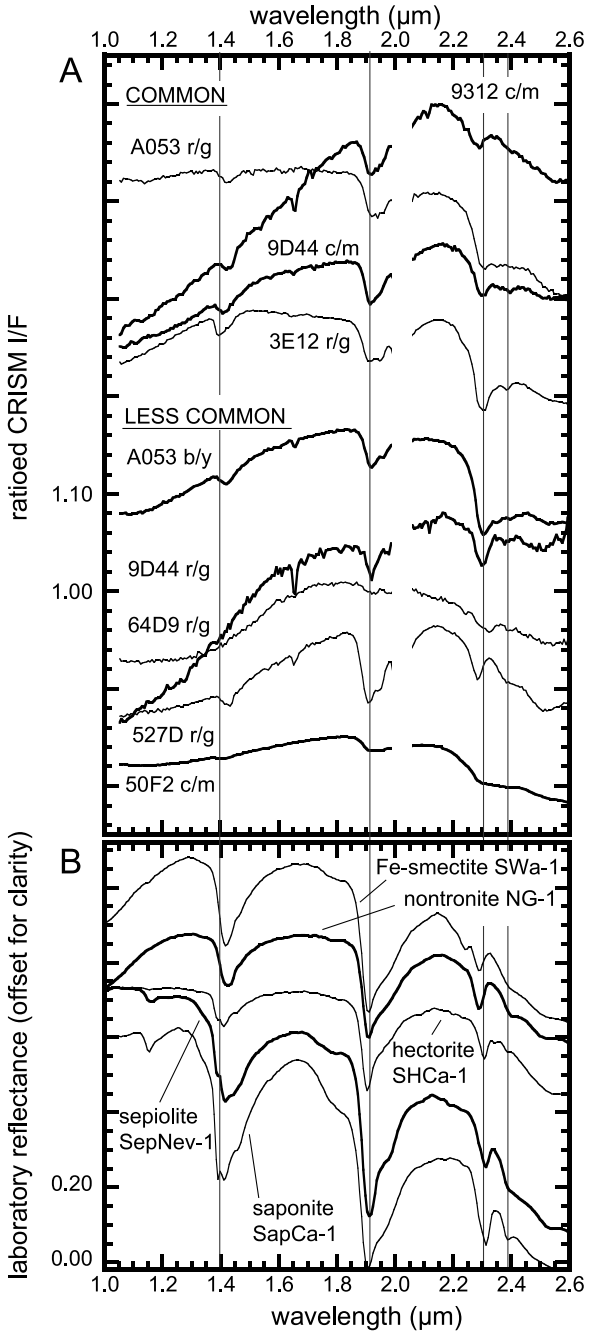

Figure 4. CRISM spectra of iron magnesium smectite-bearing materials. (a) Representative CRISM ratio spectra from numerous images throughout Nili Fossae (four-character identifier provided; for full information, see Appendix A, and for location, see Figure 3) grouped by the frequency of occurrence for spectra with those characteristics. (b) Library spectra for iron magnesium smectites and sepiolite shown for comparison. Vertical lines at 1.4 and 2.3 μm indicate absorptions which shift in position as the proportion of iron versus magnesium in smectite clays changes. The vertical line at 1.91 μm indicates the presence of H_2O and the 2.39-μm absorption indicates an OH combination tone. For details on spectra used, see Appendix A.

band depth to a broad L-shaped shoulder (e.g., 50F2 c/m and A053 r/g in Figure 4). Most Fe/Mg smectites in the Nili Fossae region exhibit an absorption centered at 2.30 μm, intermediate between the Fe and Mg end-members (e.g., 3E12 r/g and 9D44 c/m, Figure 4). This contrasts with the mostly nontronite-like spectra that are areally dominant in and around Mawrth Vallis [Noe Dobrea et al., submitted manuscript, 2009]. Yet spectra that exhibit absorptions at 2.29 μm are not uncommon, found mostly in craters to the west of Nili Fossae and in Nilo Syrtis (e.g., 9312 c/m, 527D, respectively). In many cases, these are paired with weaker absorptions near 2.4 μm. Spectra with absorptions near 2.32 μm are also found but less commonly (e.g., 64D9 r/g).

[20] A defining feature of smectites is that molecular water in the interlayer is a necessary part of the mineral structure. The strength of the ~1.9-μm band in spectral data is related to the degree of hydration, both in water molecules in the interlayer and surface hydration; this can vary depending on the thermal history of the smectite and the nature of the water [*Milliken and Mustard*, 2005]. Dehydration may be the cause of reduction in the strength of the ~1.9 band relative to the ~2.3-μm band in data from Nili Fossae. Additional intermixed hydrated phases, e.g., zeolite, may also enhance the 1.9-μm band without introducing additional bands in the wavelength region from 2.0 to 2.6 μm. Although the strength of the 1.9-μm band in Nili Fossae spectra shows considerable variation, the position of this band does not vary among the Fe/Mg smectites either in Nili Fossae or in laboratory data so it does not provide compositional information.

[21] On the other hand, there is significant variation in the strength and position of the 1.4-μm band within Fe/Mg smectites both at Nili Fossae and in laboratory data. Combination tones of H_2O are present at 1.41 μm as well as the structural OH stretching overtone that depends on the octahedral cation [*Bishop et al.*, 1994]. This stretching overtone occurs at 1.43 μm for 2Fe-OH [*Bishop et al.*, 2002a, 2002b; *Frost et al.*, 2002], at 1.41 for 2Al-OH [*Bishop et al.*, 2002a, 2002b], and at 1.38–1.39 μm for 3Mg-OH [*Clark et al.*, 1990a; *Bishop et al.*, 2002a, 2002b]. In the Nili Fossae region, the ~1.4-μm band varies in position from 1.39 to 1.43 μm, indicating a range of phyllosilicate chemistry. Notably, in the more nontronite-like spectra with absorptions at 2.29 μm, the OH overtone band is centered near 1.43 μm, as would be expected to result from a mostly iron-bearing smectite with dominantly Fe_2-OH bonds in the octahedral sites. In the most common Nili Fossae smectites with band centers from 2.30 to 2.31 μm, the greater proportion of Mg is indicated by the shift shortward of the ~1.4-μm band. In some spectra, the 1.4-μm band is weak to absent, which may be due to the effect of mixing with and/or coating by more opaque iron-bearing oxides, which commonly occur in association with Fe/Mg smectite clay minerals and can obscure the ~1.4-μm bands [*Swayze et al.*, 2002, 2003].

[22] The data collectively suggest diverse Fe/Mg smectites in the Nili Fossae region. Dominantly Mg smectites such as the trioctahedral smectites saponite or hectorite are indicated in most locations. Another Mg phyllosilicate, the fibrous clay sepiolite, cannot be excluded but rarely forms on Earth in large hundreds of km scale deposits such as observed in Nili Fossae. Additionally, more Fe-rich smectite clays are common in some parts of the Nili Fossae region, and these are likely nontronites. Notably, there is no spectral evidence for aluminum comprising an appreciable proportion of cation sites in Nili Fossae Fe/Mg smectites. While the relatively weak Fe_2OH and Mg_3OH bands near 2.4 μm can be discerned, neither a 2.21 μm (2Al-OH) or 2.23–2.25 μm (Al-Fe-OH) absorption related to Al has been identified as would be found in montmorillonite or in ferruginous smectites with significant aluminum (e.g., SWa-1, Figure 4b).

4.2. Chlorite and Prehnite

[23] In nearly a dozen CRISM images, mostly associated with craters west and south of Nili Fossae, a spectral class is detected with a prominent vibrational absorption centered at 2.34–2.35 μm with a shoulder at 2.26 μm. The 1.9-μm band is usually weaker than in smectites or absent, and there is typically a weak but sharp 1.40-μm band and, in some cases, an additional sharp band near 1.48 μm (Figure 5). We identify two minerals as being responsible for spectra of this character: chlorite and prehnite.

[24] Chlorites are 2:1:1 phyllosilicates with a T-O-T layer structure and a brucite-like octahedral interlayer and can form from primary (magmatic), hydrothermal, metamorphic, and diagenetic reactions. Bands from 2.2 to 2.5 μm vary depending on substitution of cations such as Al, Fe, and Mg in octahedral and tetrahedral layers. The strong absorption at 2.33–2.35 μm results from a combination of overtones of the Mg-OH stretch and bend and the 2.25–2.26 shoulder results from Al,Fe-OH or Al,Mg-OH stretching modes. This latter band, along with a greater band width at 2.33–2.35 μm distinguishes chlorite from serpentine [*Bishop et al.*, 2008b]. In chlorite, the band at 2.33–2.35 μm shifts to longer wavelengths as the proportion of iron relative to magnesium in the chlorite increases (Figure 5c) as has been reported for other chlorite bands [*King and Clark*, 1989]. In the Nili Fossae region, CRISM spectra have a strong 2.35-μm absorption, indicating the chlorite is comparatively iron-rich (Fe:Mg > ~0.5). A ferroan clinochlore (e.g., ripidolite; $(Mg, Fe^{2+})_5Al(Si_3Al)O_{10}(OH)_8$) [*Post and Plummer*, 1972] provides the best match to the CRISM spectra (e.g., for 50F2 s1b/s2b in Figure 5).

[25] Prehnite is a calcium aluminum silicate hydroxide and forms from hydrothermal or metamorphic activity under specific conditions of <3 kbar, 200–350°C, and X_{CO2} < 0.004. It typically forms in association with chlorite and pumpellyite [*Frey and Robinson*, 1999]. Previously, *Clark et al.* [1990b] identified the spectral features of prehnite in ground-based spectroscopic observations of Mars as those of scapolite but recently recognized that absorptions at 1.48 and 2.36 μm were due to prehnite contamination in their laboratory scapolite samples [*Clark and Hoefen*, 2000; *Clark et al.*, 2008]. Prehnite occurs in multiple locations in ancient Martian cratered terrains [R. N. Clark et al., manuscript in preparation, 2009], including the greater Argyre basin region [Buczkowski et al., manuscript in preparation, 2009]. The band position of 2.35–2.36 μm measured in laboratory spectral data of prehnite coincides

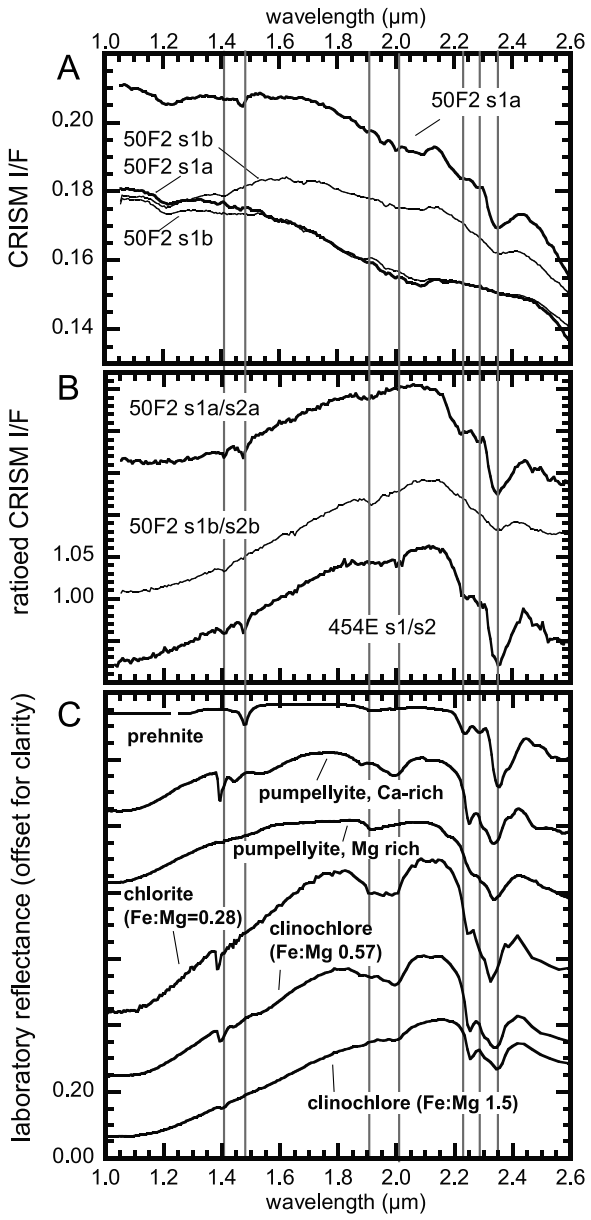

Figure 5. CRISM spectra of chlorite- and prehnite-bearing materials. (a) Unratioed CRISM spectra from FRT000050F2 (15.0°N, 72.1°E). (b) Ratioed CRISM spectra using numerators and denominators from Figure 5a and for FRT0000454E (20.1°N, 70.1°E; numerator and denominator not shown). (c) Prehnite, pumpellyite, and chlorites with varying iron content are shown for comparison. Vertical lines at 1.41, 1.48, 1.91, 2.01, 2.22, 2.28, and 2.35 μm indicate absorptions that show prehnite and chlorite are both indicated by CRISM spectra. For details on spectra used, see Appendix A.

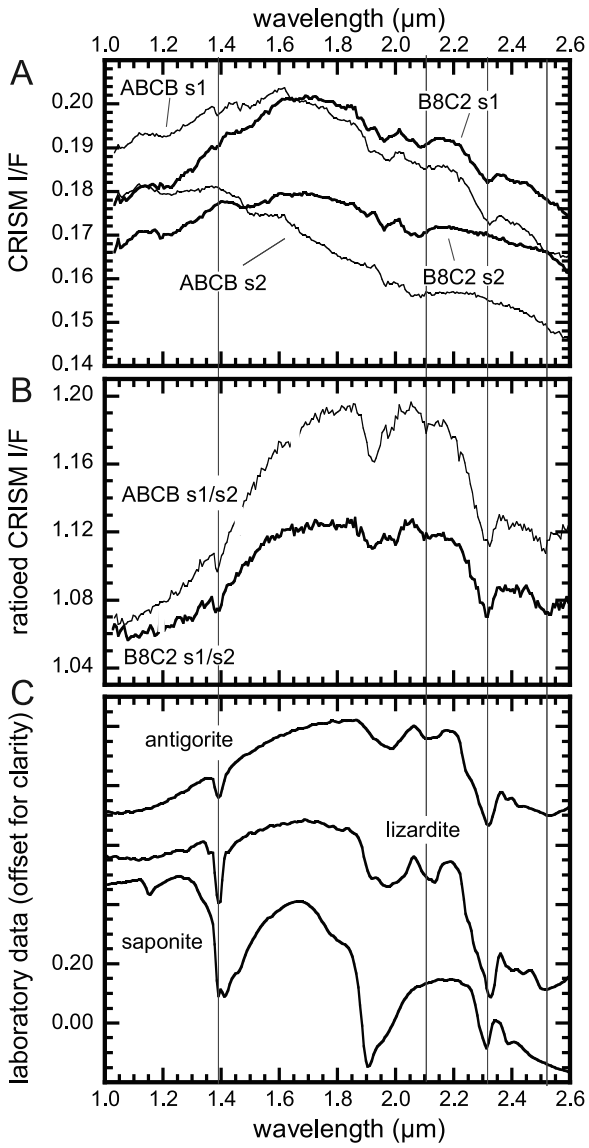

Figure 6. CRISM spectra of serpentine-bearing materials. (a) Unratioed CRISM spectra from FRT0000ABCB (thin line; 20.9°N, 73.3°E) and HRL0000B8C2 (thick line; 17.3°N, 77.1°E). (b) Ratioed CRISM spectra using numerators and denominators from Figure 6a. (c) The serpentines lizardite and antigorite and the Mg smectite saponite are shown for comparison. Vertical lines at 1.39, 2.11, 2.32, and 2.52 μm indicate absorptions that together are diagnostic of the presence of serpentine. For details on spectra used, see Appendix A.

with that of Fe-rich chlorite (Figure 5c). However, the presence of an absorption at 1.48 μm appears, from examination of numerous spectral libraries, to be uniquely diagnostic of prehnite and is the basis for identification of this mineral in the Nili Fossae region. Some CRISM spectra have absorptions at 2.35 μm, weak to absent 1.9-μm bands, and absorptions at both 1.41 and 1.48 μm (Figure 5). The continuum shape is similar to that of chlorite. We infer that spectra of this character result from a mixture of phases that include prehnite and chlorite. Pumpellyite also has a similar spectral character to chlorite, in particular more Mg-rich chlorite, but to date we do not observe a band center at 2.33 μm in the Nili Fossae spectra, so this phase cannot be positively and uniquely identified, although radiative transfer modeling results suggest its presence [*Poulet et al.*, 2008].

4.3. Serpentine

[26] A spectral class that occurs infrequently in the Nili Fossae region (two CRISM images to date) is distinguished

by an absorption centered at 2.32 μm with additional absorptions at 2.11 μm and 2.51 μm and a sharp vibrational feature at 1.39 μm (Figure 6). We identify this mineral as a magnesium-rich serpentine mineral.

[27] Serpentines are 1:1 trioctaheral phyllosilicates with the general formula (Fe, Mg)$_6$Si$_4$O$_{10}$(OH)$_8$ and form during metamorphism, hydrothermal activity, or weathering of ultramafic rocks. They have numerous combination tones of metal-OH bends and stretches from 2.3 to 2.7 μm [*King and Clark*, 1989; *Post and Borer*, 2000]. The strongest of these is centered at 2.32 μm for Mg-OH in magnesium serpentines (Figure 6c). This band has a distinctly different appearance in Fe-rich serpentines, where it occurs at longer wavelengths and is in some cases accompanied by aluminum bands at shorter wavelengths [*Calvin and King*, 1997]. The band at 2.50–2.51 μm is the next strongest of these features. Mg serpentines also have a diagnostic band at 2.10–2.12 μm. Serpentines have an OH stretching overtone located at 1.39 μm for Mg serpentines that shifts to somewhat longer wavelengths (1.40–1.41 μm) for Fe-rich serpentines [*King and Clark*, 1989; *Calvin and King*, 1997].

[28] In the CRISM spectra, from 2.0 to 2.6 μm, we observe a sharp absorption at 2.32 μm and additional absorptions at 2.51 and 2.11 μm (Figure 6). There is a 1.9-μm band indicating the presence of H_2O that is broad in the 2-μm region. There is an additional sharp vibrational band at 1.39 μm. All of these features are consistent with the presence of an Mg serpentine such as antigorite, lizardite, or chrysotile. These can be distinguished from the Mg smectite, saponite, which also has a band at 2.32 μm, by the sharpness and position of the 1.39-μm band and the additional band at 2.10 μm. Stoichiometric serpentine does not have molecular water in its structure, which would create the 1.9-μm band so we are likely observing Mg serpentine in a mixture with a hydrated phase in Nili Fossae.

4.4. Kaolinite

[29] In over a dozen CRISM images in and around Nili Fossae, a spectral class is detected that has prominent asymmetric absorptions at 1.4 and 2.2 μm (Figure 7). The 2.2-μm feature commonly occurs as a doublet with a second absorption near 2.16 μm. A 1.9-μm absorption is present but shows significant variation in strength. We identify this spectral class as a kaolinite group mineral. The doublet at 2.16 and 2.21 μm is due to a combination of vibrations of 2Al-OH groups in the mineral structure [*Clark et al.*, 1990a]. The presence of a doublet at 2.2 allows kaolinite to be distinguished from the Al-smectite montmorillonite where only a single absorption is present at 2.2 μm [*Petit et al.*, 1999]. The sharp absorption near 1.4 μm with its distinctive shoulder is also diagnostic. The particularly sharp 1.41-μm absorption in kaolin group minerals is caused by vibrations of inner hydroxyl groups between the tetrahedral and octahedral sheets leading to multiple minima near 1.4: a triplet in well-crystalline samples [*Crowley and Vergo*, 1988; *Clark et al.*, 1990a].

[30] Kaolinite group minerals are 1:1 phyllosilicates with the formula $Al_2Si_2O_5(OH)_4$ and include kaolinite and the rarer dickite, nacrite, and halloysite, the latter of which is a

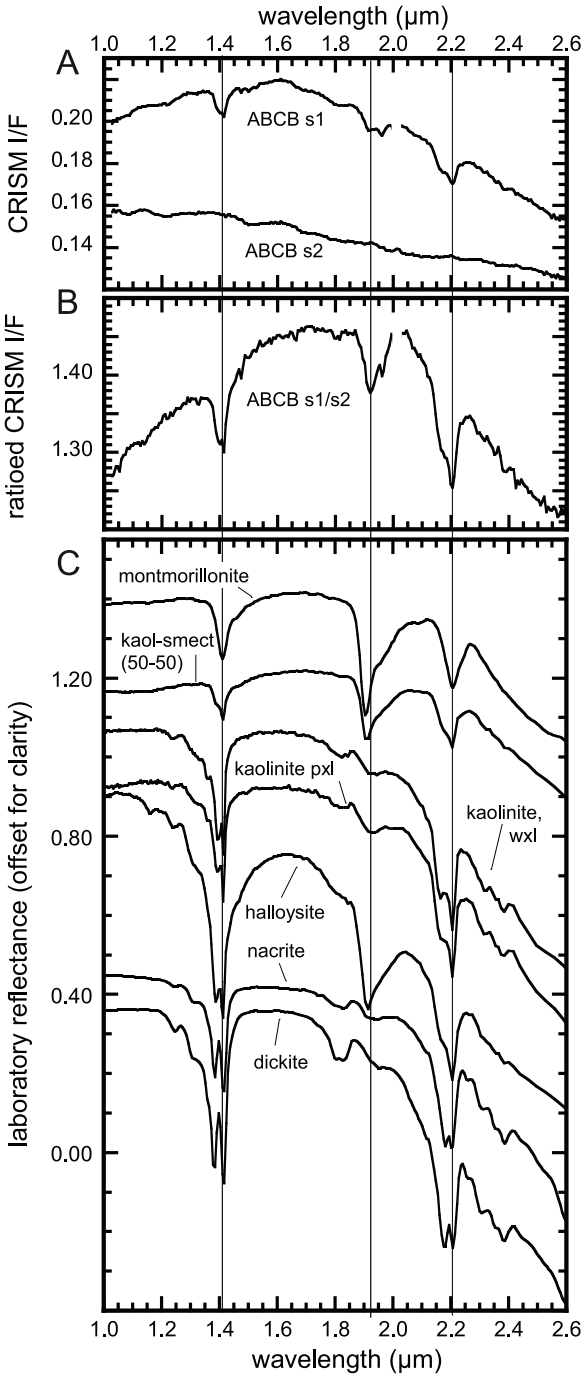

Figure 7. CRISM spectra of kaolinite-bearing materials. (a) Unratioed CRISM spectra from FRT0000ABCB (20.9°N, 73.3°E). (b) Ratioed CRISM spectrum using numerators and denominators from Figure 7a. (c) Library spectra of kaolinite group minerals and mixed kaolinite-smectite minerals show decreasing prominence of the distinctive doublet absorption with increasing crystal disorder or decreasing kaolinite content. The polymorphs dickite and nacrite can be distinguished from kaolinite and halloysite on the basis of doublet shape and band position. The vertical lines are placed at 1.4, 1.92, and 2.2 μm and indicate absorptions in CRISM data that are diagnostic of kaolinite, halloysite, or kaolinite smectite clays. For details on spectra used, see Appendix A.

hydrated form [*Giese*, 1988]. Some features in IR spectra can be used to differentiate between these similar minerals. In particular, dickite and nacrite have a prominent short wavelength absorption in the doublet at 2.17–2.18 μm whereas kaolinite and halloysite have a weaker absorption at 2.16 μm as is observed in the CRISM data from Nili Fossae (Figure 7). Kaolinite forms as a weathering product, via hydrothermal alteration, or as an authigenic sedimentary mineral [*Murray*, 1988]. The hydrated form, halloysite, usually forms under weathering or hydrothermal processes that favor a more disordered structure, such as alternating wet and dry conditions or rapid growth [*Giese*, 1988]. Well-crystalline kaolinite has a very sharp, defined doublet with two distinct absorptions at CRISM spectral resolution. Disordered kaolinite, halloysite, and kaolinite-smectite mixed layer phyllosilicates have less well-defined doublets as can be seen in Figure 7c [*Crowley and Vergo*, 1988]. CRISM spectra are generally more similar to these forms of less well-crystalline kaolinite and have a 1.9-μm band indicating structural water as is typical for halloysite and kaolinite-smectite mixed phyllosilicates. However, the separation of the doublet absorptions is near the level of noise in the CRISM data and spatial averaging to reduce noise tends to decrease the prominence of the doublet. It is also likely that a pixel might include other hydrated minerals, spatially mixed at a subpixel scale, which might contribute to the 1.9-μm band. The detection of a kaolinite group mineral is definitive, and a poorly crystalline kaolinite, halloysite or a mixed layer kaolinite-smectite (with kaolinite > smectite) are the likely specific mineral candidates.

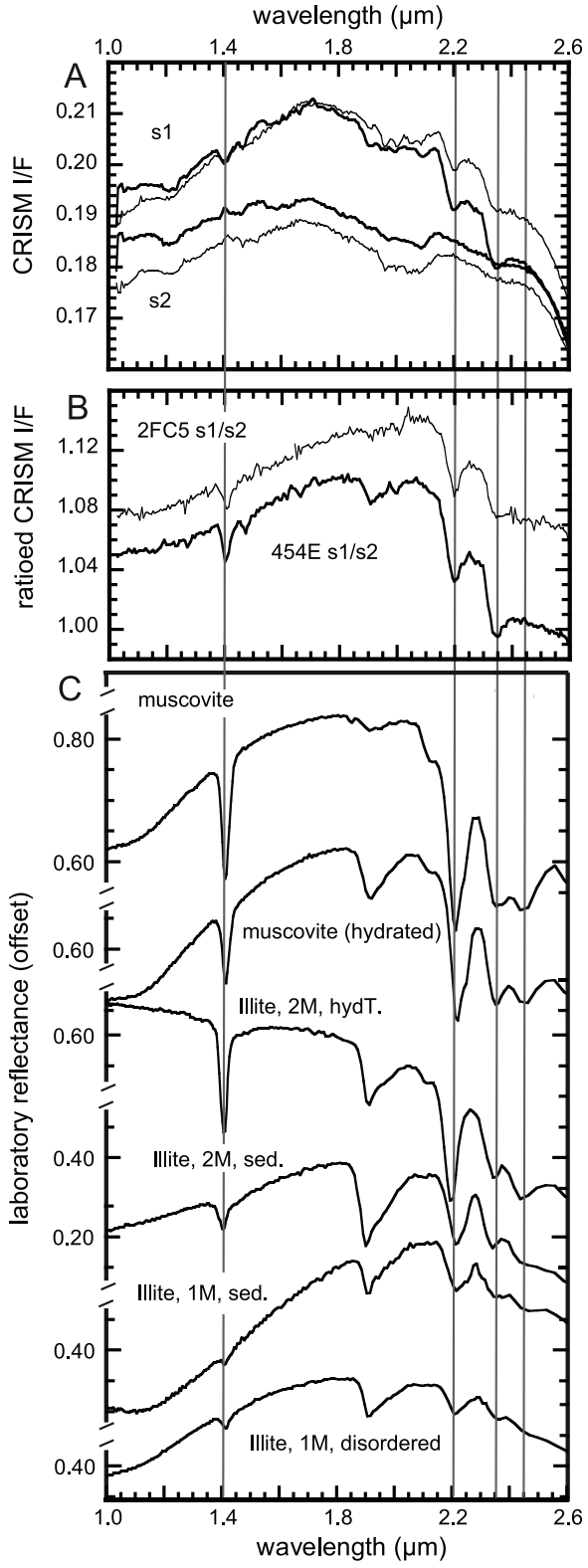

4.5. Illite/Muscovite

[31] In five CRISM images in the vicinity of a 50 km impact crater west of Nili Fossae, a spectral class is detected with sharp vibrational absorptions at 1.4, 2.2 and 2.35 μm. The 1.9-μm absorption is weak, and in some cases a weak 2.44-μm absorption is present (Figure 8). In these scenes, when the 2.2-μm feature is present, it is always accompanied by a 2.35-μm band. The strength of the 2.2-μm feature is directly proportional to the strength of the 2.35-μm band, making it unlikely the phase is a mixture.

[32] We identify this phase as a probable potassium mica. The presence of the bands at 2.2 μm, 2.35 μm and 2.44 μm distinguish K micas, i.e., illite and muscovite, from montmorillonite, which has a single absorption at 2.2 μm [*Clark et al.*, 1990a]. Additionally, the sharpness of the 1.4-μm absorption and the weak to absent 1.9-μm band indicate a phyllosilicate with little to no structural H_2O. Illite and muscovite are high layer charge (0.6–1.0), nonexpanding 2:1 phyllosilicates that contain primarily Al in the octahe-

Figure 8. CRISM spectra from K mica–bearing materials (illite or muscovite). (a) Unratioed CRISM spectra from FRT0000454E (thick line; 20.1°N, 70.1°E) and from 2 × 2 average spectra from HRS00002FC5 (thin line; 20.3°N, 70.2°E). (b) Ratioed CRISM spectra using numerators and denominators from Figure 8a. Vertical lines at 1.4, 2.2, and 2.35 μm indicate absorptions due to overtones and combination tones of metal OH–related absorptions and likely indicate the presence of a K mica such as illite or muscovite. For 454E s1/s2, a 1.48-μm band indicates an additional contribution to the spectrum from prehnite- or prehnite/chlorite-bearing materials. (c) Library spectra of K micas, i.e., illite and muscovite. For details on spectra used, see Appendix A.

dral layer, some Al in the tetrahedral layer, K in the interlayer region [*Meunier*, 2005]. The absorption features from 2.2 to 2.5 μm in K micas are due to stretch plus bend combination bands of structural OH bound to Al [*Clark et al.*, 1990a].

[33] Distinguishing between illite and muscovite is challenging. Illite is a K-deficient intermediate phase between the micas pyrophyllite ($Al_2Si_4O_{10}(OH)_2$) and muscovite ($KAl_2AlSi_3O_{10}(OH)_2$). Muscovite can be magmatic, hydrothermal, or metamorphic. Illite can form from hydrothermal, diagenetic, or weathering reactions. In diagenetic or weathering reactions, disordered or 1M polytypes of illite with significant interlayer water or mixed layer illite-smectite clays are the most common [*Rosenberg*, 2002]. With increasing temperature, pressure, or time, illite undergoes a polytypic conversion of $1M_d$ to 1M to $2M_1$ and eventually to muscovite [*Lonker and Fitzgerald*, 1990; *Rosenberg*, 2002]. NIR vibrational absorptions in spectra of these various polytypes of illite and muscovite usually differ in their relative strengths, though not positions (Figure 8c) [*Clark et al.*, 1990a; *Kruse and Hauff*, 1991].

[34] Because of the small size (<15 CRISM pixels at most) of the K mica–bearing exposures found to date, obtaining "pure" spectra of this phase is difficult. Chlorite and/or prehnite are found in the same images and in geomorphically similar knobby, ridged terrain. Their absorptions at 2.35 μm obviously contribute to the strength of the 2.35-μm feature in some K mica–bearing spectra, and the 1.48-μm absorption probably indicates the presence of prehnite (e.g., 454E in Figure 8). The 2 × 2 average spectrum from HRS00002FC5 is the "purest" found to date. The sharpness of the 1.4 and 2.2-μm absorptions, the lack of a 1.9-μm absorption, and the distinguishable 2.35 and 2.44-μm absorptions indicate K mica. The small size of exposures imaged to date and consequently relatively high noise in spectra along with the similarity of illite and muscovite in VNIR spectral data preclude a more specific identification.

4.6. Zeolite: Analcime

[35] In several CRISM images west of Nili Fossae in craters near the Antoniadi basin, spectra from small (tens of pixel at most) regions of interest have strong absorptions at 1.42 μm, 1.91 μm, and 2.52 μm and a weak absorption at 1.79 μm (Figure 9). We identify this phase as the zeolite mineral analcime.

[36] Zeolites are aluminum silicates that are made up of chains of rings of SiO_4 and AlO_4 tetrahedra. Water molecules and other cations occupy the centers of cages in the framework structure. Analcime in particular is a sodium-rich zeolite with a formula $NaAlSi_2O_6 \cdot H_2O$. It forms under hydrothermal conditions, from weathering and diagenetic reactions of igneous minerals, particularly volcanic glass, in alkaline, saline waters, and has been hypothesized to infrequently occur as a primary magmatic product [*Hay*, 1986; *Line et al.*, 1995; *Luhr and Kyser*, 1989]. NIR spectral features of zeolites are dominated by sorbed water [*Hunt et al.*, 1973; *Clark et al.*, 1990a]. However, laboratory spectra of analcime are quite distinct from those of other zeolites, even Na-rich ones such as natrolite [*Clark et al.*, 1990a; *Cloutis et al.*, 2002] (Figure 9c). Analcime is

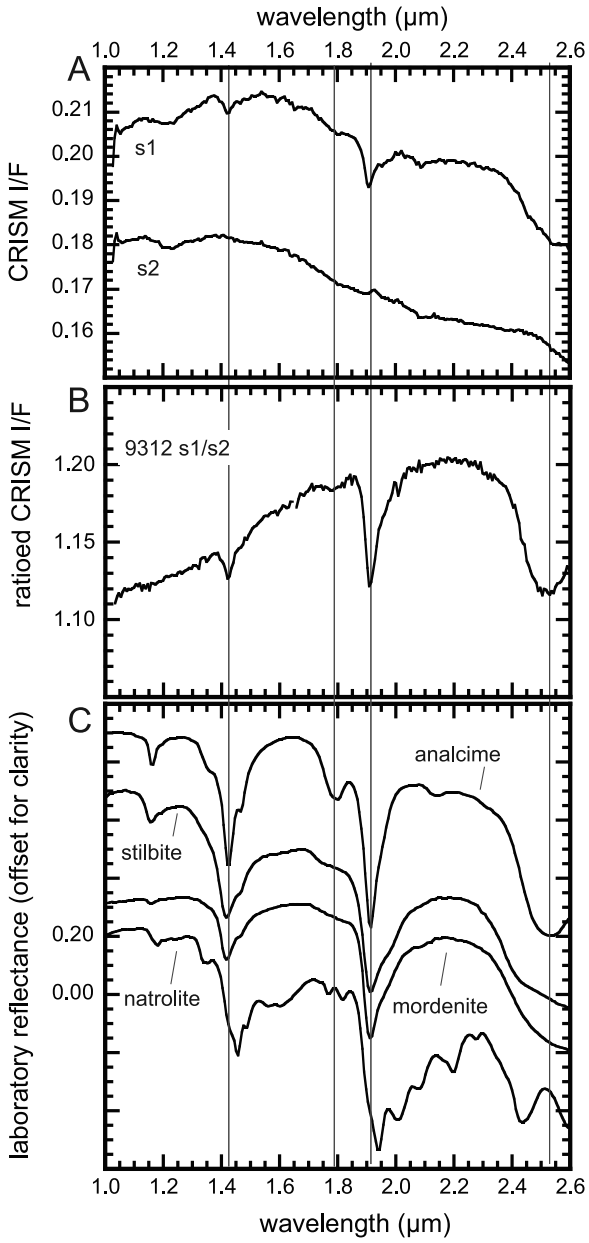

Figure 9. CRISM spectra from analcime-bearing materials. (a) Unratioed CRISM ratio spectra from FRT00009312 (19.9°N, 65.9°E). (b) Ratioed CRISM spectrum using the numerator and denominator spectra from Figure 9a. Vertical lines at 1.42, 1.79, 1.91, and 2.52 μm mark absorptions indicating the presence of analcime. (c) Library spectra of zeolites. For details on spectra used, see Appendix A.

characterized by strong absorptions at 1.42 μm, 1.91 μm, 2.52 μm and progressively weaker absorptions at 1.79 μm, 1.12 μm, 2.14 μm. The 1.79 μm band is seen in CRISM data, but the latter two are not. This may simply be a function of abundance, the weakest bands are the first to "disappear" at the SNR level as abundance decreases, or a result of Fe-related minerals obscuring the shorter wavelength features (as discussed in section 4.1 for smectites). The spectral shape and absorption band positions in the CRISM data closely match those of analcime, whose suite of absorp-

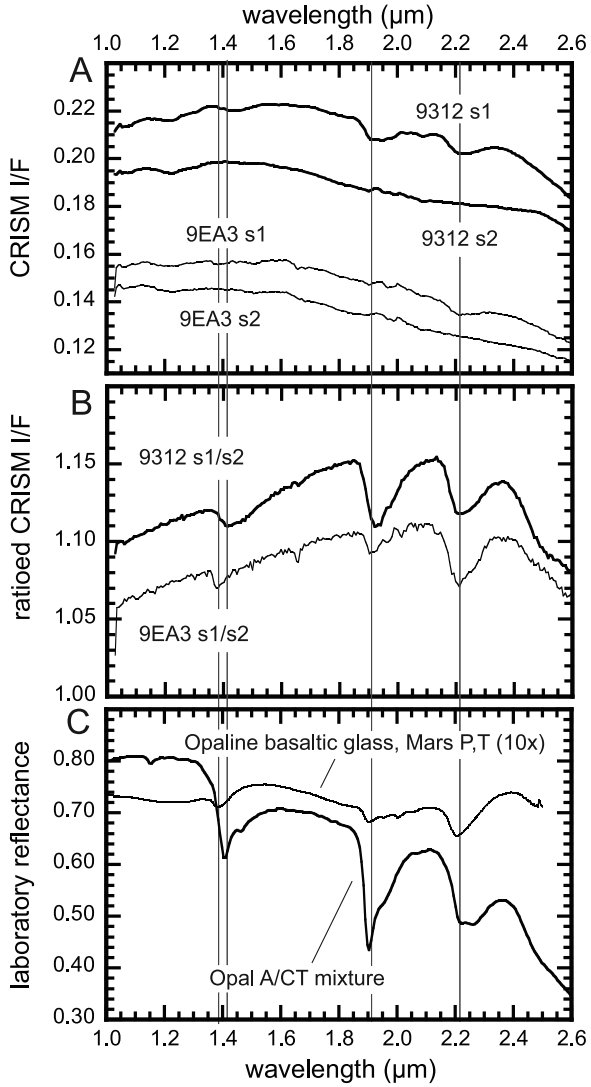

Figure 10. CRISM spectra from hydrated silica-bearing materials. (a) Unratioed CRISM spectra from FRT00009312 (thick line; 19.9°N, 65.9°E) and from HRL00009EA3 (thin line; 16.8°N, 71.6°E). (b) Ratioed CRISM spectra using numerators and denominators from Figure 10a. (c) Library spectra of basaltic glass with an opaline coating measured under Mars pressure and temperature conditions (reflectance scaled by a factor of 10) [*Swayze et al.*, 2007] and opal-A/CT [*Clark et al.*, 2007]. The vertical line at 1.91 μm shows the location of an absorption indicating the presence of H_2O. Vertical lines at 1.39, 1.41, and 2.21 μm show the positions of absorptions that indicate Si-OH bonds and the presence of hydrated silica, e.g., opal, with differing degrees of hydration. For details on spectra used, see Appendix A.

tions in this wavelength range are apparently unique among minerals measured by NIR spectroscopy to date.

4.7. Hydrated Silica

[37] In over a dozen CRISM images taken within craters in the Nili Fossae region and over topographic ridges within the Antoniadi basin, a phase occurs with a broad absorption at 2.2 μm and also absorptions at 1.4 μm and 1.9 μm (Figure 10). We identify this phase as hydrated silica, which has been previously described in detail for layered deposits near Valles Marineris [*Milliken et al.*, 2008].

[38] Opaline silica and hydrated (H_2O bearing), hydroxylated (OH bearing) basaltic glass exhibit absorption bands due to combination tones of Si-OH at 2.21–2.22 μm due to isolated Si-OH and at 2.26 μm due to H-bound Si-OH [*Anderson and Wickersheim*, 1964; *Stolper*, 1982; *Goryniuk et al.*, 2004]. These bands near 2.2 μm are clearly wider than those observed in aluminum phyllosilicates [*Milliken et al.*, 2008]. The bands at 1.91 μm are due to H_2O in the mineral structure whereas those near 1.4 μm result from both H_2O and structural OH. The 1.4-μm band position in both opal and hydrated basaltic glass is near 1.40–1.41 μm [*Langer and Florke*, 1974; *Stolper*, 1982], although this can shift shortward to as much as 1.38 μm when only the influence of the Si-OH bond remains, following the removal of H_2O [*Anderson and Wickersheim*, 1964; *Swayze et al.*, 2007; *Milliken et al.*, 2008]. With less water, the influence of the 2.26-μm band is also diminished resulting in a narrowing in the 2.2-μm band.

[39] In Nili Fossae, we observe spectra with a broad absorption centered near 2.21 μm with a 1.41-μm band position as well as spectra with a broad but slightly narrower absorption at 2.21 μm with a weaker 1.9-μm band, and a 1.39-μm band (Figure 10c). These spectra are consistent with hydrated silica with varying amounts of H_2O in the structure. The former is more consistent with opal, i.e., hydrated amorphous silica; the latter is more consistent with a partially dehydrated opal or altered basaltic glass.

4.8. Other Zeolites or Polyhydrated Sulfate Mixtures

[40] In four CRISM images to date from the Nili Fossae region, spectra have been collected with stronger water-related bands at 1.43 μm and 1.92 μm than commonly observed in most other Martian terrains bearing hydrated minerals (Figure 11). These spectra also display very subtle absorption features at 2.20 μm, 2.26 μm, and 2.42 μm.

[41] As discussed above, absorptions near 2.20 μm and 2.26 μm may indicate the presence of opaline phases or hydrated, hydroxylated glasses. However, the band positions in the CRISM data are at 1.43 μm and 1.93 μm, i.e., shifted longward from typical locations for these bands in hydrated silica. Along with the weakness of the bands near 2.2 μm, this suggests a mixture of phases for this spectral class. The dominance of water-related bands in the spectrum and the absence of other diagnostic bands precludes a precise mineral identification at present. As discussed above, NIR spectral features of zeolites are dominated by sorbed water [*Hunt et al.*, 1973; *Clark et al.*, 1990a] as are spectral features in polyhydrated magnesium and ferric sulfates [*Cloutis et al.*, 2006] (Figure 11c). The positions of the 1.43-μm and 1.92-μm bands in the CRISM data best match those of a zeolite. Absorptions near 1.4 and 1.9 μm in sulfates are usually at longer wavelengths. However, in a sulfate-opaline silica mixture, broader bands with centers intermediate between sulfate and silica might be expected. A very subtle inflection is seen in CRISM data at 2.4 μm. This absorption occurs in the Group 5 structural class of zeolites and may be an H_2O combination band [*Cloutis et al.*, 2002] but also occurs in spectra of some polyhydrated

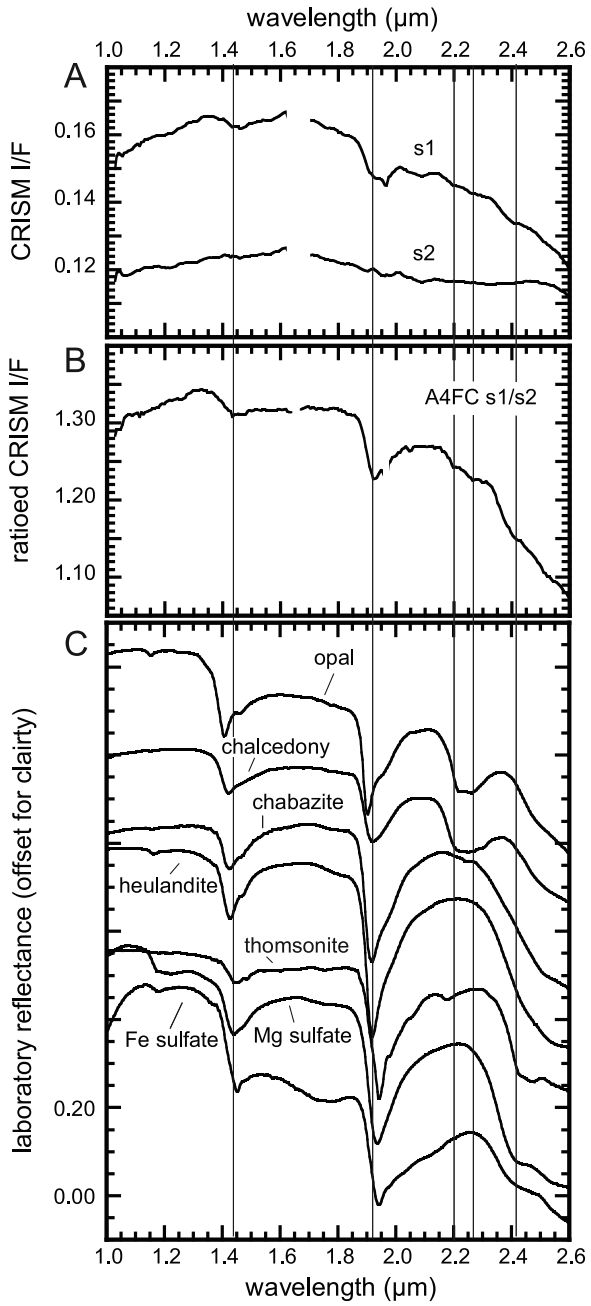

Figure 11. CRISM spectra from mixed hydrated silica-bearing materials. (a) Unratioed CRISM ratio spectra from FRT0000A4FC (22.0°N, 77.2°E). (b) Ratioed CRISM spectrum using the numerator and denominator spectra from Figure 11a. (c) Library spectra of opal, zeolites, and polyhydrated sulfates for comparison (CRISM spectral library, measured by *Cloutis et al.* [2002] and *Clark et al.* [2007]). Vertical lines are at 1.43, 1.93, 2.20, 2.26, 2.42 μm and, as discussed in the text, the observed absorption features do not unambiguously identify a single mineral but probably indicate a mixture of hydrated silica with either sulfates or zeolites. For details on spectra used, see Appendix A.

Fe and Mg sulfates [*Cloutis et al.*, 2006]. While the mineral identification for this spectral class of hydrated material is currently indeterminate, the most likely candidates are either a silica-zeolite or a silica-sulfate mixture.

4.9. Carbonate

[42] In over two dozen images in the eastern portion of Nili Fossae, spectra with paired absorptions at 2.31 and 2.51 μm are observed. These characteristic spectra also have a 1.9-μm band and a broad absorption centered near 1.0 μm (Figure 12). This phase is identified as magnesium carbonate as detailed by *Ehlmann et al.* [2008a].

[43] Paired absorptions of equivalent strength at 2.3 and 2.5 μm are overtones of the fundamental absorptions of carbonate that occur in the 6–15 μm range [*Lane and Christensen*, 1997], and the precise wavelengths of the minima depend on the cation paired with the carbonate [*Hunt and Salisbury*, 1971; *Gaffey*, 1987]. Magnesite or a mixture of hydromagnesite+magnesite provide the best spectral match to the band shape and position of the 2.31 and 2.51-μm bands observed in CRISM spectra (Figure 12c). The carbonate phase we see is in some cases clearly in a mixture and contains a hydrous component, either hydrous carbonate or another constituent. Iron magnesium smectites have a strong absorption at 2.3 μm and successively weaker absorptions at 2.4 and 2.5 μm (nontronite, Figures 12c; Figure 4). The presence of a small additional feature at 2.4 μm, sometimes present with the carbonate (e.g., A09C, Figure 12b), probably indicates the presence also of Fe/Mg smectite, either spatially or intimately mixed. The broad absorption at 1.0 μm is due to ferrous iron either in small amounts in the magnesite or in associated olivine [*Ehlmann et al.*, 2008a].

[44] In contrast to most hydrated silicates, carbonate also has diagnostic absorptions in the 3–4 μm range, specifically broad absorptions at 3.4 and 3.9 μm. CRISM data from Nili Fossae in carbonate-bearing terrains show a strong 3.9-μm absorption band and a considerably weaker 3.4-μm absorption (Figure 12e) [*Ehlmann et al.*, 2008a]. The 3.4 μm band may be weakened or distorted by what is apparently an instrumental artifact centered at 3.18 μm [*Murchie et al.*, 2009a], which does not map coherently with geomorphic units either here or elsewhere on the planet and does not correspond to known absorptions in library spectra. The 3.4 and 3.9-μm bands in carbonate are in some cases quite strong and of equivalent strength (e.g., Mag. CB-EAC-006A, Figure 12f); however, sometimes the 3.4 μm band may be considerably weaker than the 3.9-μm band (e.g., Mag CC-JFM-006B and mag.+hydromag., Figure 12f). The natural variability of these band strengths is not well studied. Grain size may play a role, and water can also act to subdue bands in the 3–4 μm range. In hydrous carbonates, bands from 3 to 4 μm may be entirely absent (Figure 12f) [*Calvin et al.*, 1994].

[45] Unratioed CRISM spectra have a strong positive slope at wavelengths greater than ~3.5 μm due to the thermal emission contribution of the surface. The 3.9-μm band can be distinguished as an inflection, or slightly reduced steepness over wavelengths >3.7 μm, in carbonate-bearing materials relative to noncarbonate-bearing materials (Figure 12d). The strongest 3.9-μm absorptions map

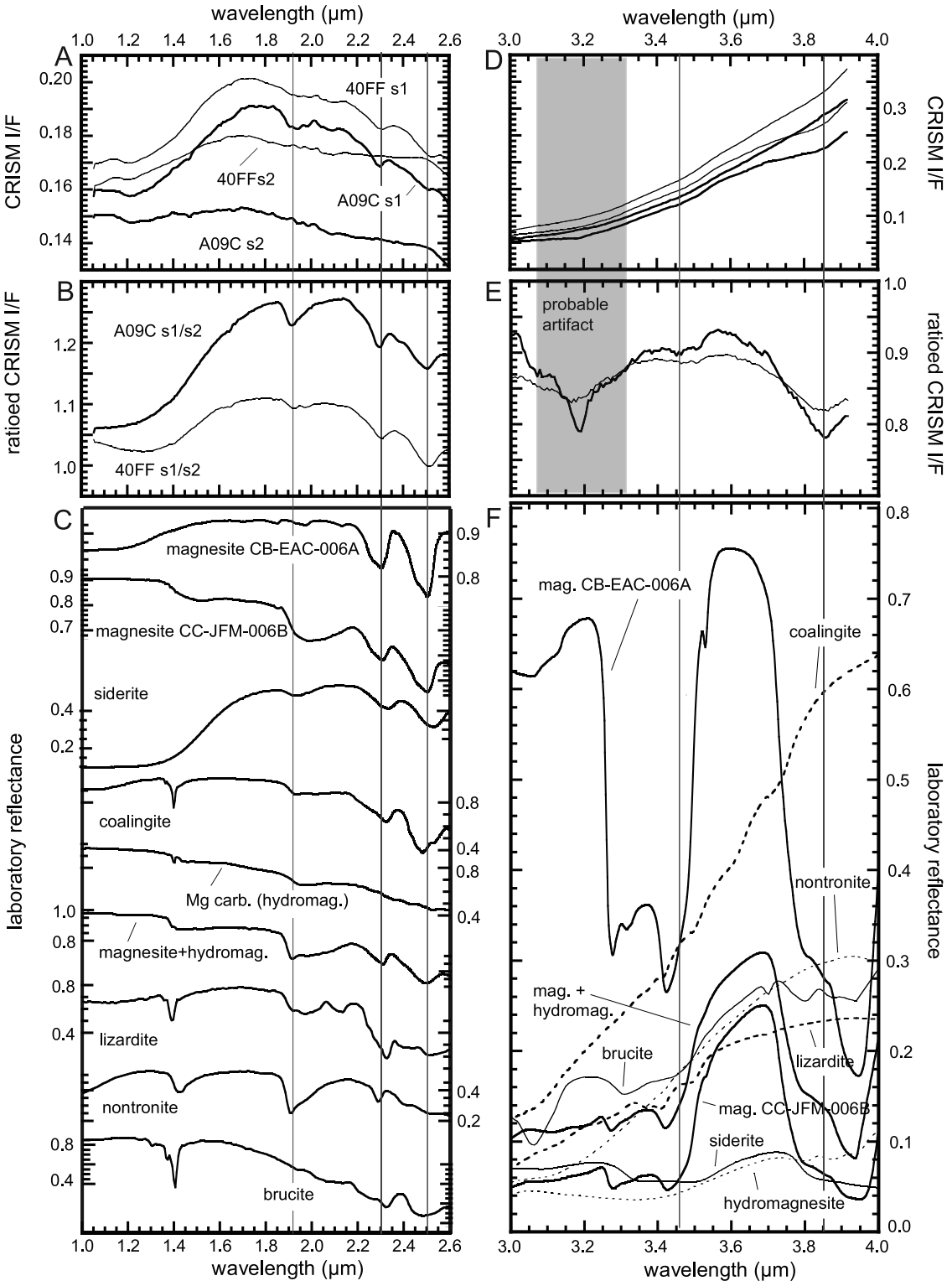

Figure 12. CRISM spectra from magnesium carbonate–bearing materials. (a) Unratioed CRISM spectra from FRT0000A09C (thick line; 21.3°N, 78.5°E) and FRT000040FF (thin line; 18.5°N, 77.4°E). (b) Ratioed CRISM spectra using the spectra from Figure 12a as numerators and denominators. (c) Library spectra of carbonates and hydrated silicates shown for comparison. The vertical lines in Figures 12a–12c are at 1.93, 2.31, and 2.51 μm, respectively, indicating the presence of H_2O and the two absorptions due to carbonate. (d–f) Same as Figures 12a–12c but over the 3–4 μm wavelength range. The vertical lines in Figures 12d–12f are at 3.46 and 3.85 μm, indicating the two absorptions due to carbonate. The wavelengths impacted by a probable detector artifact are shown in gray. For details on spectra used, see Appendix A.

spatially in the same locations as the 2.31 and 2.51 μm bands [*Ehlmann et al.*, 2008a, supplementary online material]. The 2.51-μm band never occurs alone in spectrally sampled terrains in this part of the planet but is always accompanied by the 2.31 μm band. These spectral characteristics allow magnesium carbonate to be identified and mapped.

5. Geomorphology and Geologic Setting

5.1. Mineral Distribution: Provinces of Alteration

[46] With the higher spatial resolution provided by CRISM, hydrated minerals in the greater Nili Fossae region are detected extending further westward than previously known from analysis of OMEGA data [*Mangold et al.*, 2007; *Mustard et al.*, 2007]. Examination of Figure 2 shows that Fe/Mg smectites are the most common alteration mineral in the Nili Fossae region, as is true of Mars globally. Fe/Mg smectites are nearly ubiquitous in Noachian terrains. They are detected in targeted images over the entire study area except in the Hesperian Syrtis Major lava flows, dust-covered terrains north of Baldet crater, and east of the Nili Fossae where the uppermost unit is Amazonian Isidis basin fill.

[47] In contrast to the consistent presence of the Fe/Mg smectites, other hydrated minerals show considerable heterogeneity in distribution. Kaolinite and carbonate are found only in the area immediately around the Nili Fossae, with carbonate specifically restricted to the easternmost part of the area (Figure 2). In and around impact craters, especially to the west and south of Nili Fossae, different alteration minerals are observed, especially chlorite and prehnite. From crater to crater, there are distinct mineralogic assemblages, i.e., combinations of mineral-bearing units detected in the same geographic area. For example, a 50 km crater (20°N, 69°E) has a prehnite-chlorite-K mica assemblage whereas two 25 km impact craters (19°N, 65°E) have a smectite-chlorite-hydrated silica-analcime assemblage, while Toro crater (17.0°N, 71.9°W) has a Fe/Mg smectite-chlorite-prehnite-silica assemblage.

[48] Below, we consider in greater detail the geomorphology of the mineral-bearing units for each alteration mineral identified. In accordance with the distinctive mineralogic assemblages identified and their distinctive geomorphic set-

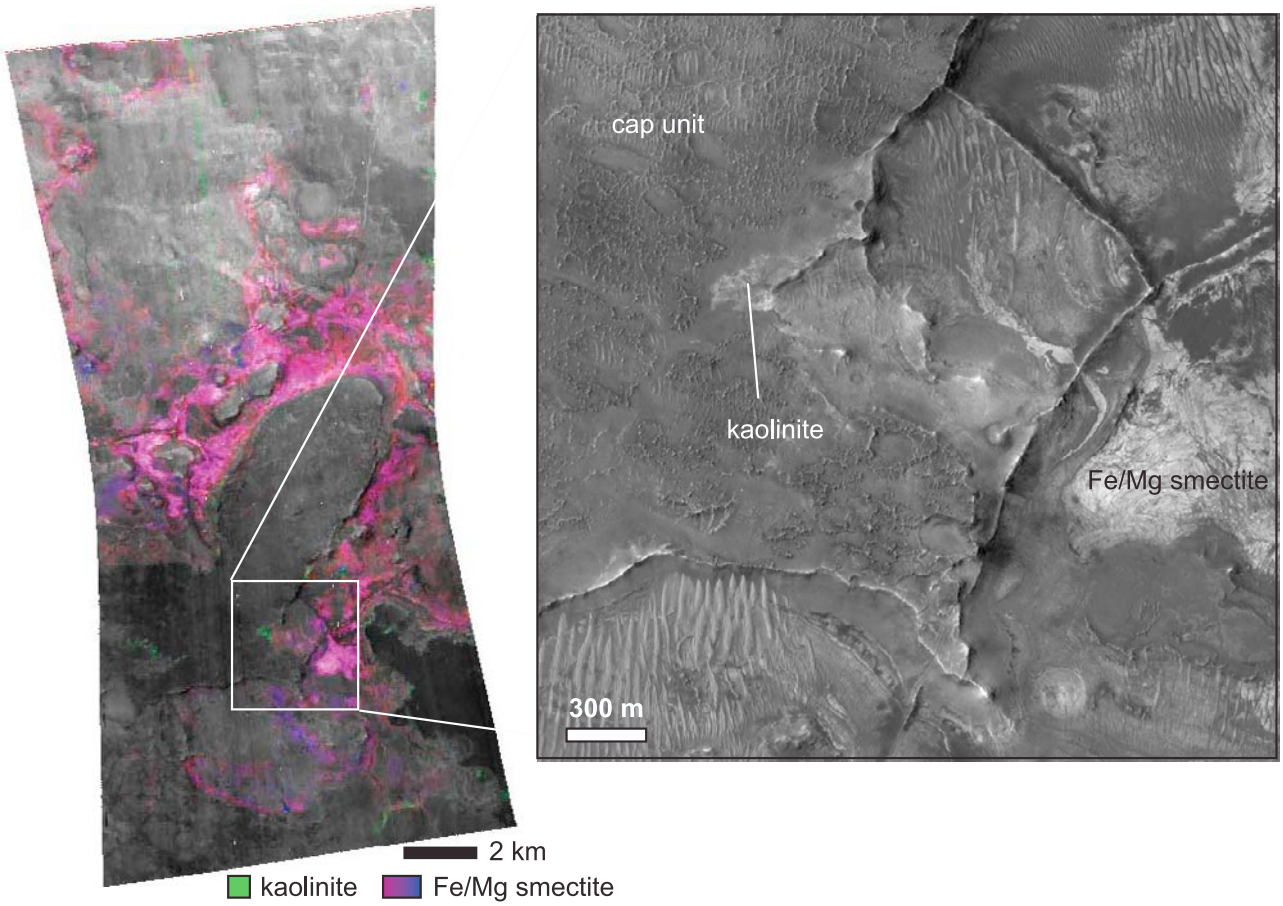

Figure 13. Stratigraphy of kaolinite- and smectite-bearing units west of Nili Fossae. CRISM HRL0000B404 (21.8°N, 72.3°E) infrared albedo map colorized with parameter maps (red, BD1900H; green, BD2200; blue, D2300) so that Fe/Mg smectite–bearing materials are magenta to blue and kaolinite-bearing materials are green. A close-up view of the contact between the cap, Fe/Mg smectite–bearing unit, and largest exposure with kaolinite is shown in a subset of HiRISE image PSP_008993_2020_RED.

tings discussed below, we divide the region into provinces of alteration: Eastern, Western, and Central/North Syrtis.

5.2. Eastern Province: Nili Fossae Stratigraphy

[49] Like OMEGA data, CRISM data show Fe/Mg smectite–bearing rock units are the lowermost exposed stratigraphic unit, i.e., the basement rock, in eastern Nili Fossae [*Mangold et al.*, 2007; *Mustard et al.*, 2007, 2008]. From 72°E to 80°E, smectite-bearing basement rock is well exposed by erosion in numerous locations, including in a 600 m thick section of the walls of the largest Nili Fossae trough. As discussed further by *Mustard et al.* [2009], this Fe/Mg smectite–bearing unit may represent megabreccia constituting the early Noachian Martian crust. It is composed of variably altered blocks bearing Fe/Mg smectite and low-calcium pyroxene in a smectite-bearing matrix. When eroded, the brecciated unit commonly exhibits linear ridges, which may represent former conduits of fluid flow. Some Fe/Mg smectite–bearing materials have also undergone sedimentary transport and are a component in layered deposits cropping out in mesas in northern Nilo-Syrtis chaos, filling the fossae, filling impact craters, and forming deltaic deposits in Jezero crater [*Mustard et al.*, 2009; *Ehlmann et al.*, 2008b].

[50] The distribution of kaolinite is mostly restricted to the eastern portion of the study area, in and around the Nili Fossae. Kaolinite-bearing units occur as a distinctively bright-toned layer, always on top of the Fe/Mg smectite–bearing units. The kaolinite-bearing layer overlies both types of Fe/Mg smectite–bearing deposits: massive crustal smectites as well as layered sedimentary smectites. West of the Nili Fossae, Figure 13 shows a thin (tens of meters thick at most) layer of kaolinite-bearing material being exposed by the erosion of an overlying caprock unit that lacks a mineralogically distinct spectral signature in CRISM data but is the highest stratigraphic unit in and around the Nili Fossae [*Mustard et al.*, 2009]. The kaolinite-bearing unit overlies a much thicker, ridged Fe/Mg smectite–bearing unit. Hundreds of miles to the east, kaolinite-bearing units also overlie massive crustal phyllosilicates. Figure 14 shows a kaolinite-bearing unit overlying a smectite-bearing unit along the wall of Nili Fossae trough, a 5 km long portion of which has been faulted and forms a downdropped slump block. The kaolinite occurs in a bright toned unit, well exposed beneath a mostly removed thin mantle. The kaolinite is exposed in a contiguous area elevated ~80 m relative to its surroundings in MOLA DEM data, although without a higher-resolution topographic model for the surface it is difficult to determine the dip and thickness of the kaolinite-bearing unit; 80 m should be considered an upper bound. The kaolinite-smectite stratigraphy is present even on the downdrop block, indicating kaolinite formation likely predates the fossae opening or at least the last significant tectonic activity.

[51] Just to the northwest of this scarp is a 40 km crater that is over 1 km shallower than a nearby counterpart of the same diameter owing to significant sedimentary fill (Figure 15). A CRISM image acquired over an eroded pit in the center of the crater shows that although most of the fill is Fe/Mg smectite–bearing (A053, Figure 4a), the uppermost ~20 m of the exposed stack of fill has the distinctive spectral signature of kaolinite (Figure 15c). Interestingly,

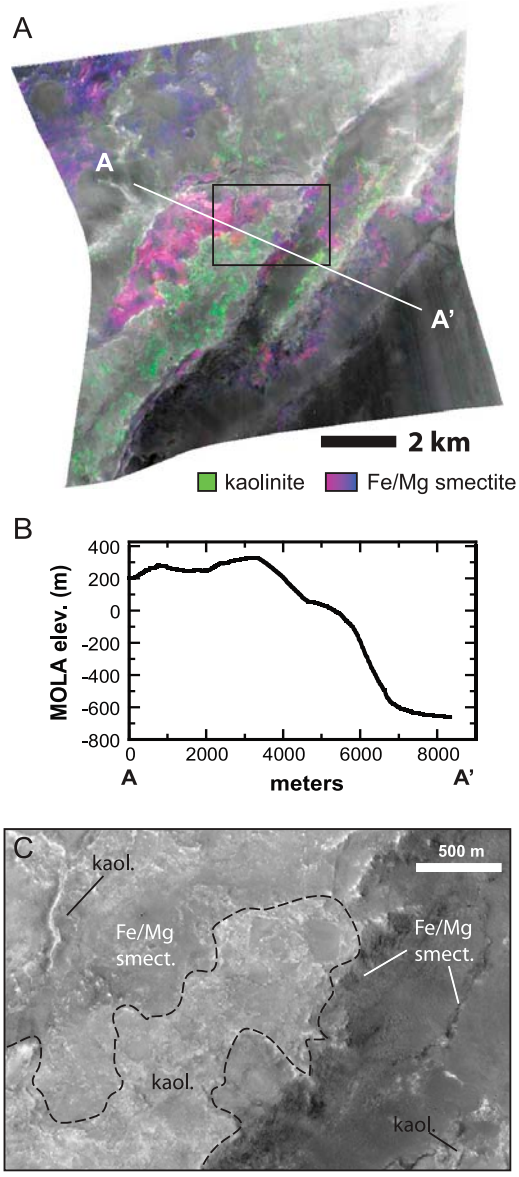

Figure 14. Stratigraphy of kaolinite- and smectite-bearing units along Nili Fossae trough. (a) CRISM FRT00009971 (22.1°N, 74.6°E) infrared albedo map colorized with parameter maps (red, BD1900H; green, BD2200; blue, D2300) so that Fe/Mg smectite–bearing materials are magenta to blue and kaolinite-bearing materials are green. (b) Profile extracted from the MOLA DEM (CRISM DDR band 10) across the trough scarp from the line A–A′ in Figure 14a, showing a 900 m scarp with a distinctive downdropped block. (c) A subset of HiRISE image PSP_006989_2025_RED showing the black box in Figure 14a at higher resolution. The kaolinite-bearing unit corresponds to the outlined brightest-toned units which also have some blocks of low-calcium pyroxene (not shown in Figure 14a).

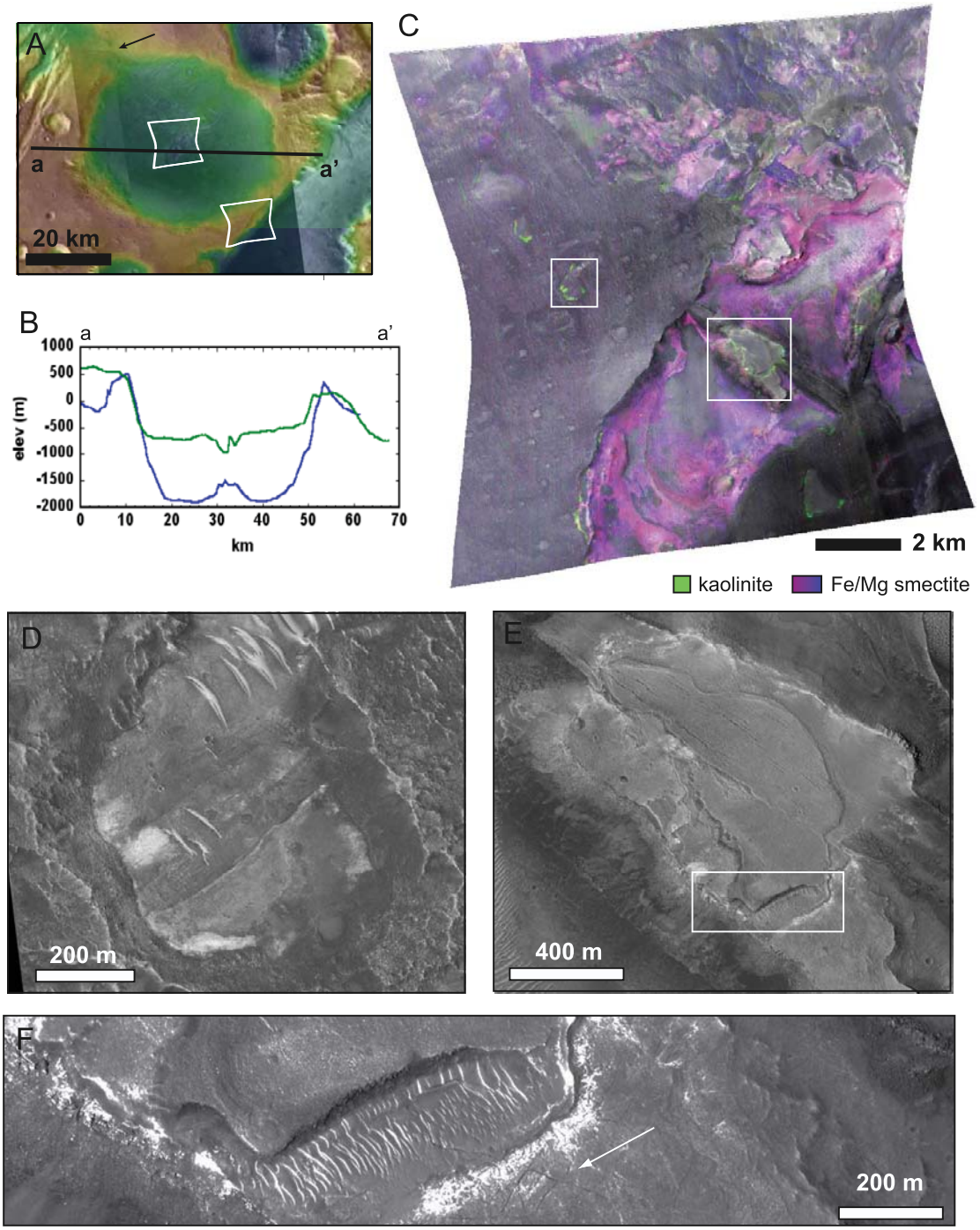

Figure 15. Kaolinite-bearing units overlying sedimentary Fe/Mg smectite–bearing units. (a) MOLA digital elevation model with the outlines of CRISM image FRT0000A053 (22.4°N, 74.3°E) within the crater over the eroded central pit and FRT00009971 (Figure 14) over the Nili Fossae trough scarp to the southeast. The arrow indicates the location of the channel draining the crater. (b) In MOLA elevation profiles, the crater of interest (green) is ~1 km shallower than nearby Hargraves crater (blue: 20.7°N, 75.8°E), a fresher crater of the same diameter, because of sedimentary fill. (c) CRISM FRT0000A053 infrared albedo map colorized with parameter maps (red, BD1900H; green, BD2200 and D2300) so that Fe/Mg smectite–bearing materials are magenta to blue and kaolinite-bearing materials are green. The image was acquired over an area of eroded crater fill in the central pit, and the phyllosilicates are exposed by this erosion. (d and e) Close-up views of exposures of kaolinite-bearing materials from the white boxes in Figure 15c with HiRISE image PSP_007345_2025_RED. Materials which are kaolinite-bearing (green in Figure 15c) are bright. (f) Close-up view of white box in Figure 15e showing the lack of bedding in the bright kaolinite-bearing units. The arrow indicates fractures in overlying mantling material.

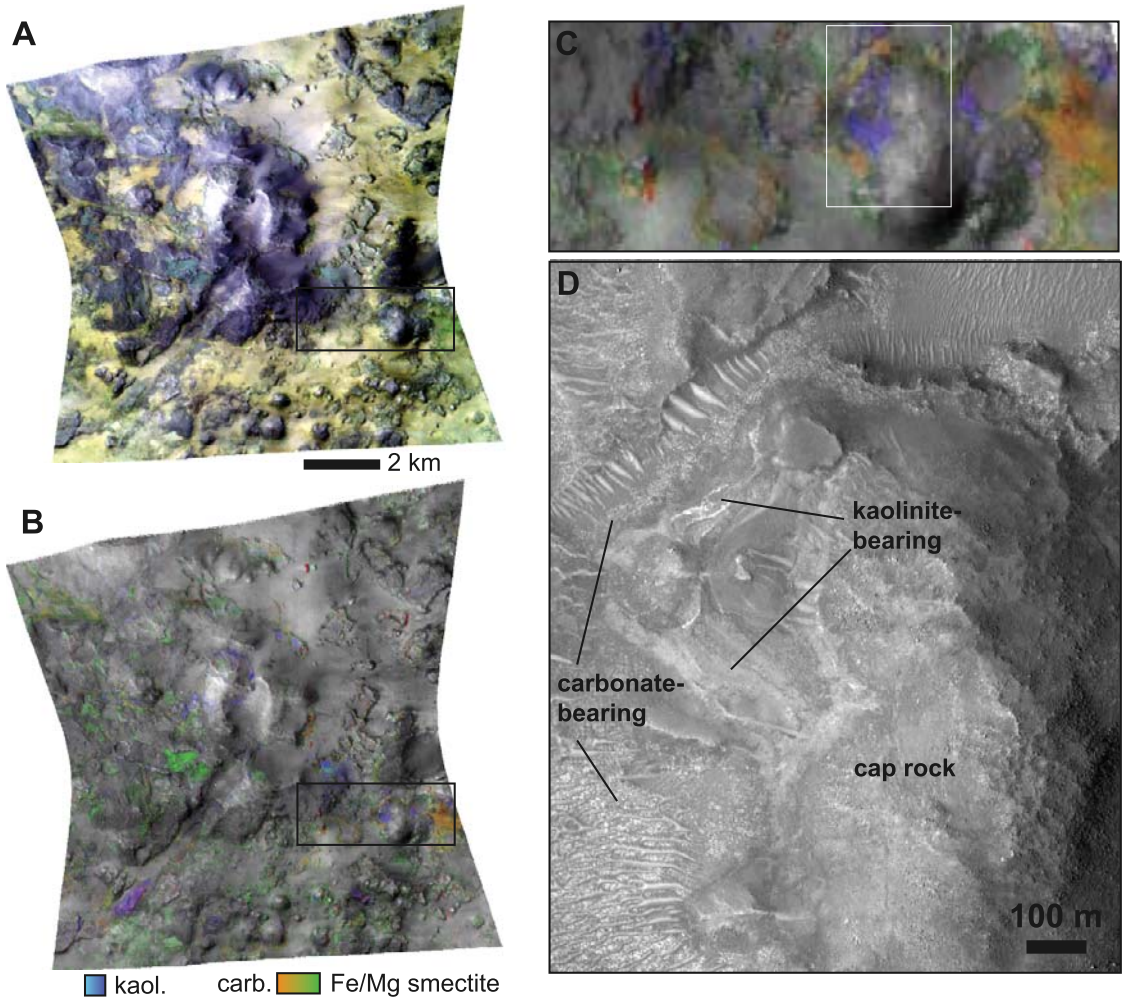

Figure 16. Stratigraphy of carbonate-bearing unit, kaolinite-bearing unit, and caprock in eastern Nili Fossae. (a) CRISM FRT0000A09C (21.3°N, 78.5°E) false color composite image (red, 2.38; green, 1.80; blue, 1.15 μm) in which olivine is yellow, phyllosilicates are cyan, and carbonate is green. (b) Parameter map (red, BD2500; green, D2300; blue, BD2200) where kaolinite-bearing units are blue to purple, Fe/Mg smectite–bearing units are green, and Mg carbonate–bearing units are yellow to orange. (c) Close-up view of the black box in Figure 16b. (d) Subset of HiRISE PSP_002321_2015_RED showing the stratigraphy of carbonate- and kaolinite-bearing units beneath the caprock.

as in observations of kaolinite over massive crustal Fe/Mg smectite–bearing terrains, no bedding can be discerned in the kaolinite-bearing unit. The kaolinite unit in some cases does have a fractured appearance, as in Figure 15f, where the fractures appear to extend into an overlying thin mantle. However, along with its stratigraphic position, the unit's most characteristic trait is that the kaolinite-bearing materials are typically 5–15% brighter than surrounding materials in both infrared albedo at 1.3 μm (IRA parameter) [*Pelkey et al.*, 2007] and reflectance at 0.77 μm (R770).

[52] In the easternmost portion of Nili Fossae, 76°E to 80°E, the occurrence of kaolinite is less common. Instead, beneath a capping unit but above Fe/Mg smectites are olivine-bearing rocks [*Mustard et al.*, 2008, 2009] that have in places been altered, in some cases to magnesium carbonate [*Ehlmann et al.*, 2008a]. To date, only one imaged location contains both carbonate- and kaolinite-bearing units in a distinctive stratigraphy. In this image, it appears that a bright kaolinite-bearing unit overlies a polygonally fractured carbonate-bearing rock unit (Figure 16), which is partially obscured by olivine sands derived from the regional olivine bedrock unit [*Hamilton and Christensen*, 2005; *Mustard et al.*, 2008]. Further imagery to assess the kaolinite-carbonate relationship will be sought.

[53] As discussed by *Mustard et al.* [2009] the olivine-bearing rocks in eastern Nili Fossae drape preexisting topography and fill in topographic lows. Figure 17 shows the typical three-unit stratigraphy observed: (1) Fe/Mg smectite–bearing units are overlain by (2) olivine-bearing rocks, which in some places are altered and contain Mg carbonate, and are in turn overlain by (3) a caprock which lacks a mineralogically distinctive signature in CRISM data. In this particular location, a crater was formed in Fe/Mg smectite–bearing units, subsequently filled and covered by the olivine-bearing and caprock units, and then eroded by surface fluvial activity that formed a valley draining into one of the fossae to the southeast. Exposed, ridged Fe/Mg smectite megabreccia is capped by mesas of banded olivine

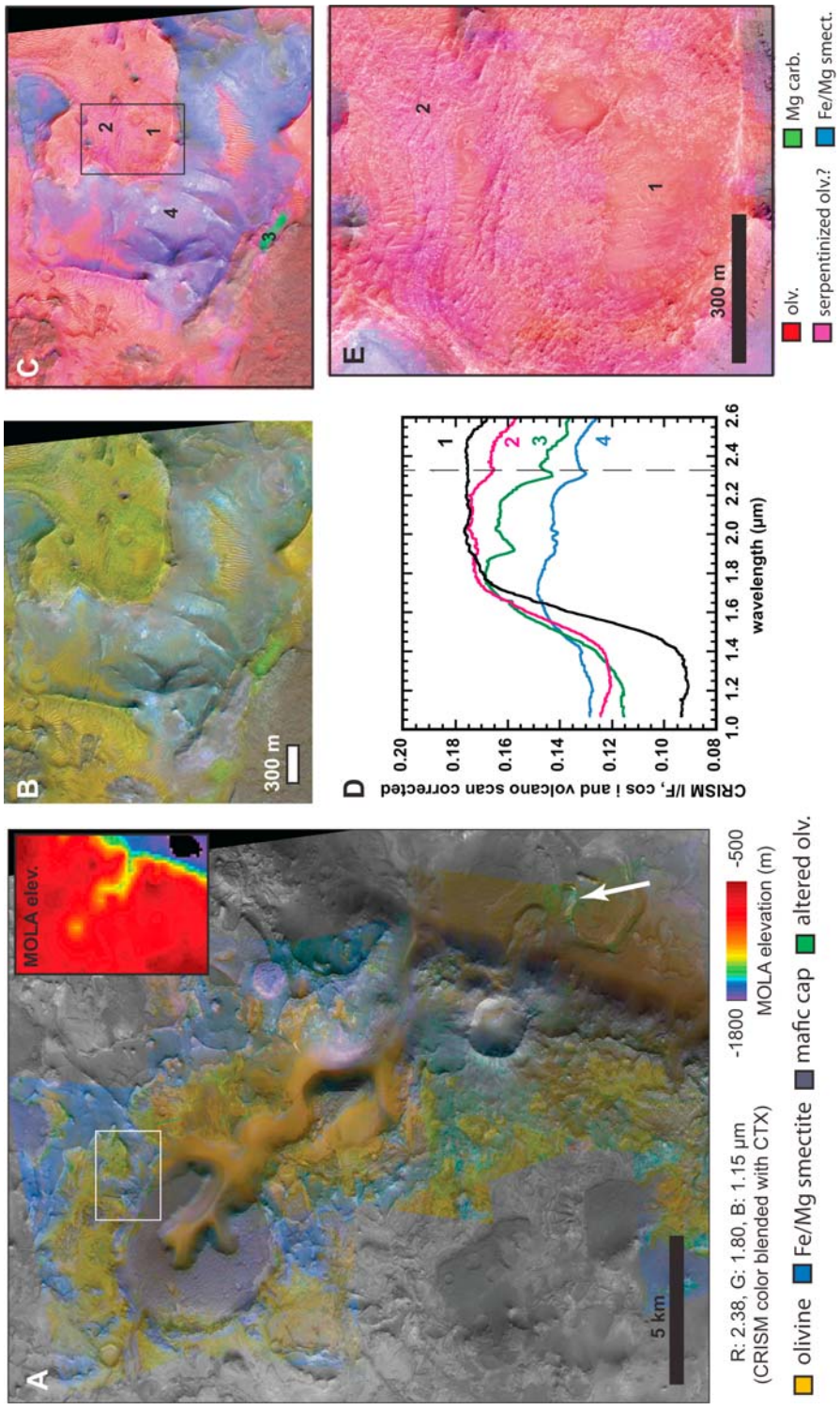

Figure 17. Carbonate-, smectite-, and olivine-bearing rocks in eastern Nili Fossae. (a) False color CRISM images FRT00003E12, FRT0000B438, FRT0000A4FC, and FRT0000871C (red, 2.38; green, 1.80; blue, 1.15 μm) near 22.1°N, 77.1°E were used to colorize a portion of grayscale CTX image P03_002176_2024_XI_22N283W_070113. With this choice of bands, olivine appears yellow, Fe/Mg smectites are blue, and altered olivine (sometimes what is spectrally distinctly carbonate) is green. An arrow indicates a bright white/cyan patch which has a spectral signature of the mixed hydrated phase discussed in the text (silica+zeolite or silica+sulfate; Figure 11). A MOLA elevation map showing the topography of the scene is inset. (b) CRISM data from Figure 17a was used to colorize a subset of HiRISE PSP_002888_2025_RED shown in the white box in Figure 17a. (c) Same HiRISE subset colorized with a CRISM parameter map (red, OLINDEX; green, BD2500; blue, D2300). The red and blue channels are scaled by $((G_{scene\ max.} - G)/G_{scence\ max.})$ so that carbonate-bearing units are green rather than white. Red is olivine, and blue is Fe/Mg smectite. Noncarbonate altered olivine is magenta. (d) Unratioed CRISM spectra from the units labeled 1–4 in Figure 17c. (e) Close-up view of Figure 17c showing the banded, partially altered olivine-bearing rocks beneath olivine sands.

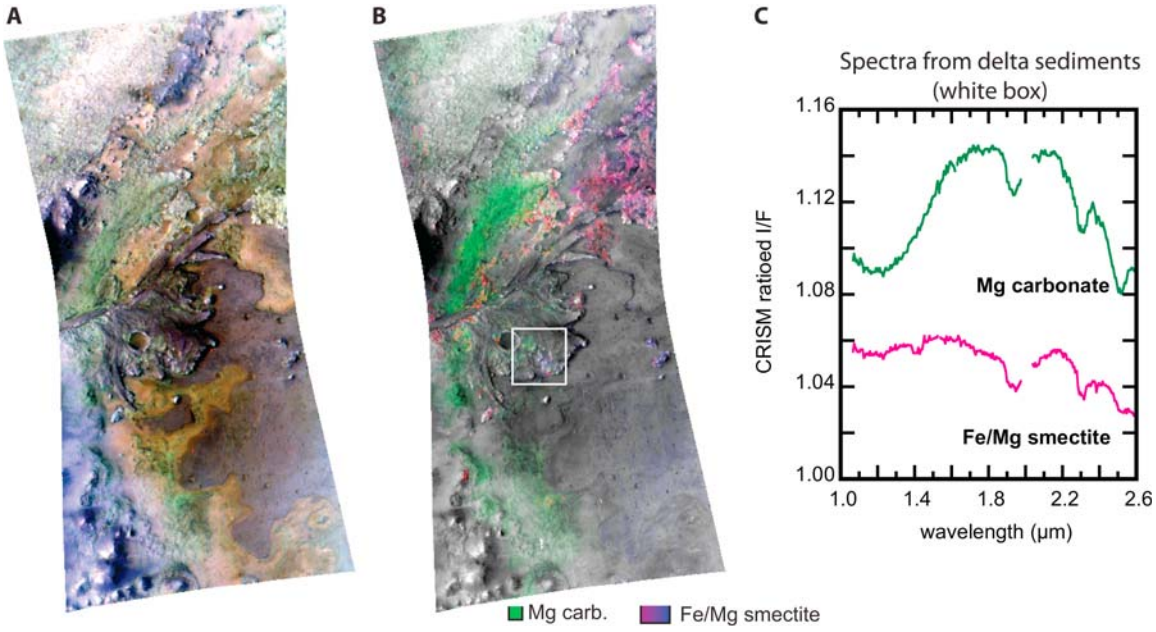

Figure 18. Transported carbonate-bearing and Fe/Mg smectite–bearing materials in Jezero crater. (a) False color CRISM image HRL000040FF (18.5°N, 77.4°E) with colors as in Figure 16. (b) Parameter map (red, D2300; green, BD2500; blue, BD1900H). For each pixel, the red and blue channels are scaled by the value of the green channel $((G_{scene\ max.} - G)/G_{scence\ max.})$ so that predominantly carbonate-bearing units appear green rather than white. Magenta to blue units are more Fe/Mg smectite enriched. (c) CRISM ratioed spectra from regions of interest from light-toned deltaic sediments within the box shown in Figure 18b. Spectra from each region were ratioed to the same denominator spectrum.

overlain by a caprock without a distinctive mineralogic signature (Figure 17). Around the margins of the cap, where water is likely to have flowed, these units have in some places altered to Mg carbonate (green, Figure 17c). However, some of the olivine shows signs of alteration of a different nature (magenta in Figures 17c–17e) with an absorption centered at 2.32 μm. This absorption occurs at a wavelength too long to be Fe/Mg smectite, which has its absorption at 2.30–2.31 μm (3E12, Figure 4a) and lacks the 2.5-μm absorption, which is characteristic of carbonate (Figure 17d). The band centers of these spectra are more similar to saponite or to the serpentine observed elsewhere in eastern Nili Fossae. To date, serpentine has only been definitively identified in two images in very small exposures in and around the fossae (Figures 2 and 6). One is in FRT0000B8C2 where it seems contiguous with olivine- and Mg carbonate–bearing rocks. The second, in heavily eroded terrain in FRT0000ABCB does not correlate with a distinctive unit in a stratigraphy.

[54] Immediately around the Nili Fossae, alteration phases are also sometimes associated with fluvial features. Mg carbonate and Fe/Mg smectite are found in the valleys feeding into Jezero crater and in transported sediments within the Jezero crater deltas. Jezero crater is a 45 km crater, filled with sedimentary deposits and fed by a 15,000 km^2 catchment, which is thought to have hosted a paleolake [*Fassett and Head*, 2005; *Ehlmann et al.*, 2008b]. Figure 18 shows the relative distribution of carbonate versus smectite near Jezero crater's western delta, which extends outward from a valley to the west (not pictured the image). Spectra from light-toned units in the well-formed western delta appear to indicate packages of distinctive composition, some more Mg carbonate enriched and another more Fe/Mg smectite enriched (Figures 18b and 18c). The clearest carbonate signatures, those least contaminated by smectite, found to date are from HRL000040FF and rocks draped on the western wall of Jezero crater that underlie the western delta (Figure 12). The northern delta appears somewhat more Fe/Mg smectite enriched than the western delta, although all sediments probably contain both alteration minerals. Magnesium carbonate is also found near an eroded fluvial channel in the Nili Fossae (green in Figure 17a). This same channel (arrow to cyan, Figure 17a) hosts the hydrated mixed phase (silica + zeolite or silica + sulfate; Figure 11).

5.3. Western Cratered Province

[55] In the far west of the study area, along the eastern margin of the Antoniadi basin (62° to 67°E), a distinctly different suite of alteration minerals occurs, accompanying iron magnesium smectite (Figure 2). Chlorite is typically found as is hydrated silica. In two craters, the distinctive spectral signature of analcime has also been observed.

[56] In this area, the Fe/Mg smectite and chlorite are found in bedrock units. In four CRISM images acquired within the Antoniadi basin, chlorite and smectite occur in knobs and ridges extending over several kilometers, which have been embayed by younger units with no distinctive mineralogic signature in NIR data. In two 25 km impact craters, chlorite and smectite are found in the central peak. The northernmost crater shows the brecciated nature of the central peak (Figure 19) with 100 m angular boulders set in

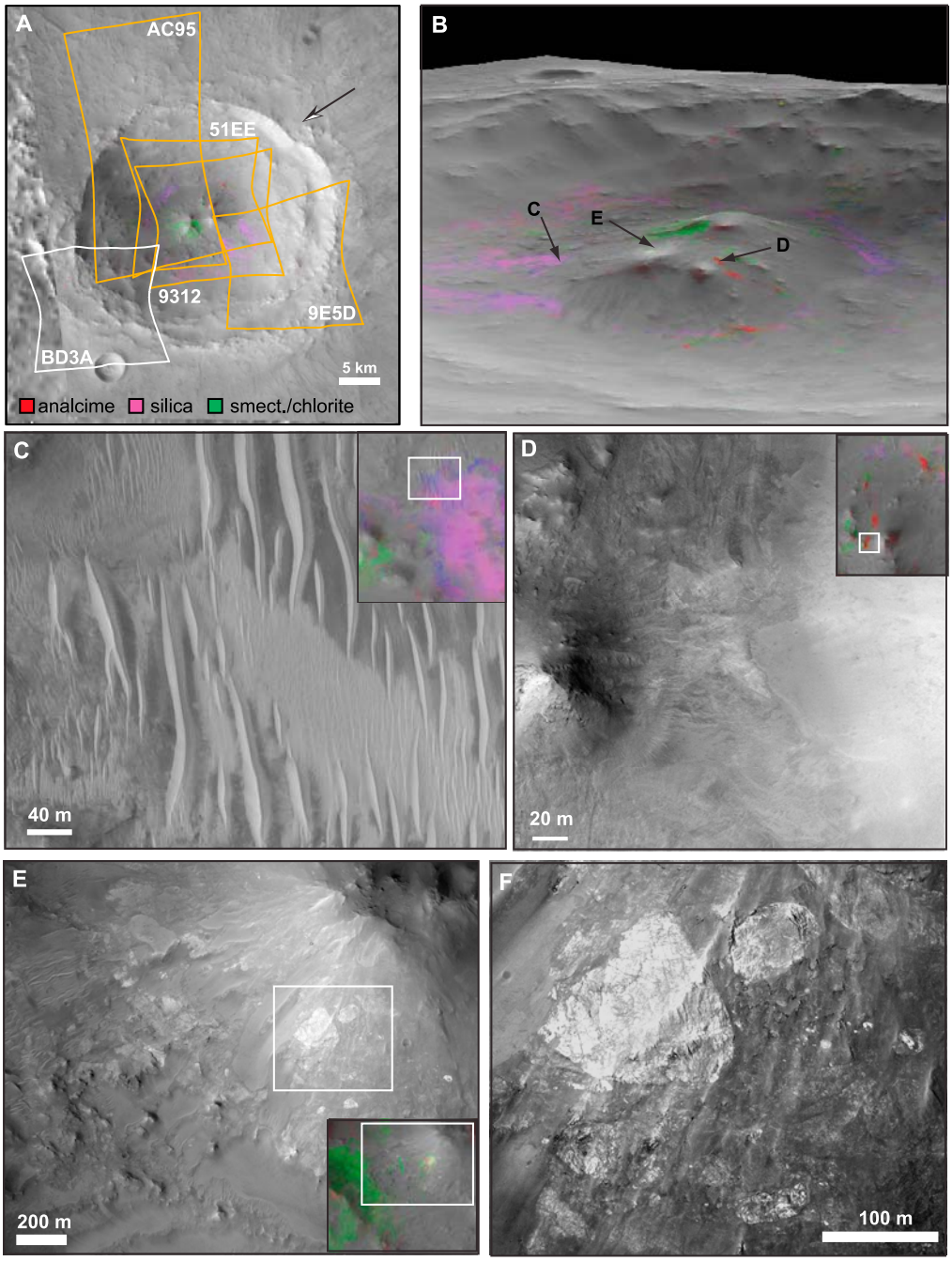

Figure 19. Mineral maps from a 25 km crater west of Nili Fossae near 20°N, 66°E. (a) CTX image mosaic colorized with mineral maps (red, BD2500; green, D2300; blue, BD2200) from CRISM images FRT000051EE, FRT00009312, FRT00009E5D, FRT0000AC95, and FRT0000BD3A overlain. Materials bearing the zeolite analcime are red, hydrated silica are magenta, and Fe/Mg smectite and chlorite are green. The arrow shows the viewing perspective for Figure 19b. (b) Three-dimensional perspective view (3X vertical exaggeration) of the distribution of minerals within the crater provided by draping Figure 19a over a MOLA digital elevation model. (c–e) Subsets of HiRISE image PSP_003205_2000_RED showing in greater detail regions bearing hydrated silica, zeolite, and Fe/Mg smectite, respectively, taken from areas indicated in the inset images and in Figure 19b. (f) Close-up of the area shown by the white box in Figure 19e showing breccia blocks composing the central peak materials.

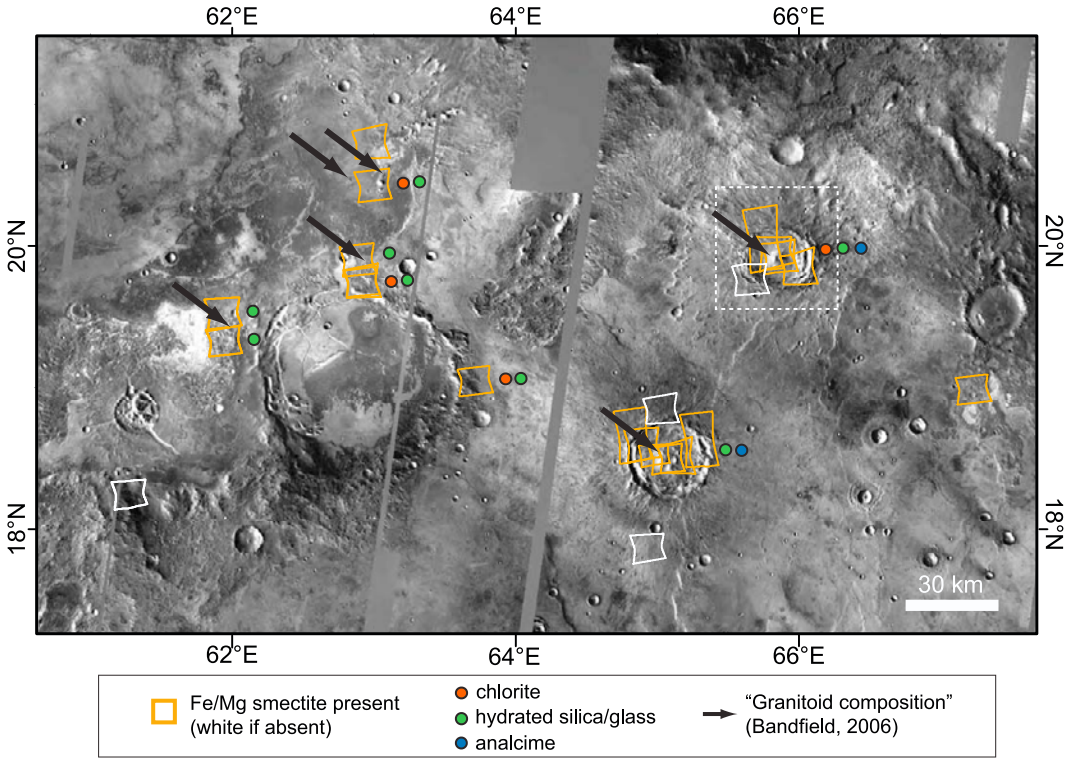

Figure 20. THEMIS day infrared mosaic with black arrows indicating the locations of TES/THEMIS-identified granitoid/quartzofeldspathic materials from *Bandfield* [2006] along with minerals identified by CRISM. CRISM observation outlines and mineral detections within CRISM images are shown as in Figure 2. The dashed white box indicates the location of Figure 19. The locations of the granitoid materials correspond to CRISM detections of hydrated silica.

a rock matrix. The mineralogic signature of smectite and chlorite appears in both blocks and matrix material. Whether spectra appear more chlorite-like or Fe/Mg smectite-like varies spatially but does not appear to correspond to unique geomorphic units. Within the northern 25 km crater, chlorite/smectite is also found in rocks exposed on the southwestern crater wall (Figure 19b). Although most chlorite-bearing materials in the region around the Nili Fossae also have a 1.48-μm band indicative of the presence of prehnite, the chlorite in these craters lacks this prehnite spectral feature (Figure 5b).

[57] Within the two 25 km craters, the sodium zeolite analcime (Figure 9) is found in rocks in and around the central peak (Figure 19). The size of zeolite-bearing outcrops is comparatively small, no more than a few tens of CRISM pixels. In some cases, the physical properties of zeolite-bearing rocks are distinctive. Figure 19d shows analcime in brighter-toned rocks being exhumed from beneath a smooth covering material that lacks a mineralogically distinctive signature. In other places, analcime is found associated with large boulders at the base of the central peak.

[58] The occurrence of hydrated silica is common throughout this part of the study area; however, to date this phase has not been found in any rock unit. Rather, the hydrated silica is found in mobile materials. In the northern 25 km crater, hydrated silica occurs in a ring around the central peak, which HiRISE imaging shows is a mobile unit of aeolian dunes and ripples (Figure 19c; 9312 in Figure 10). Smaller patches of hydrated silica-bearing sands are located in local depressions and along scree slopes on the southern wall of the 25 km crater and within the Antoniaidi basin. Interestingly, the locations of the hydrated silica correspond to the locations identified by *Bandfield* [2006] using Thermal Emission Spectrometer (TES) and THEMIS data, as units of granitoid or quartzofeldspathic composition (Figure 20). Materials ringing the crater central peak mapped as quartzofeldspathic [*Bandfield et al.*, 2004] correspond to the aeolian materials mapped with CRISM as hydrated silica.

5.4. Central Province: North Syrtis Craters

[59] In craters located near the margins of the Syrtis Major flow immediately west and south of Nili Fossae, chlorite and prehnite are the areally dominant alteration minerals, and Fe/Mg smectites are considerably less prevalent. In contrast to the craters in the Western province, the less areally abundant phases present within each of these craters vary considerably among craters. The northernmost of the craters has associated K mica while the southernmost craters have hydrated silica or, outside of the crater, kaolinite (Figure 2).

[60] Figure 21 shows a 50 km diameter crater at the northern margin of the Syrtis Major lava flows. High-resolution images indicate that the crater of interest was formed after emplacement of the Hesperian Syrtis Major formation; its ejecta overlie unaltered Syrtis Major lavas that fill a crater to the southeast. The crater of interest either formed by an impact into the side of a hill or has been

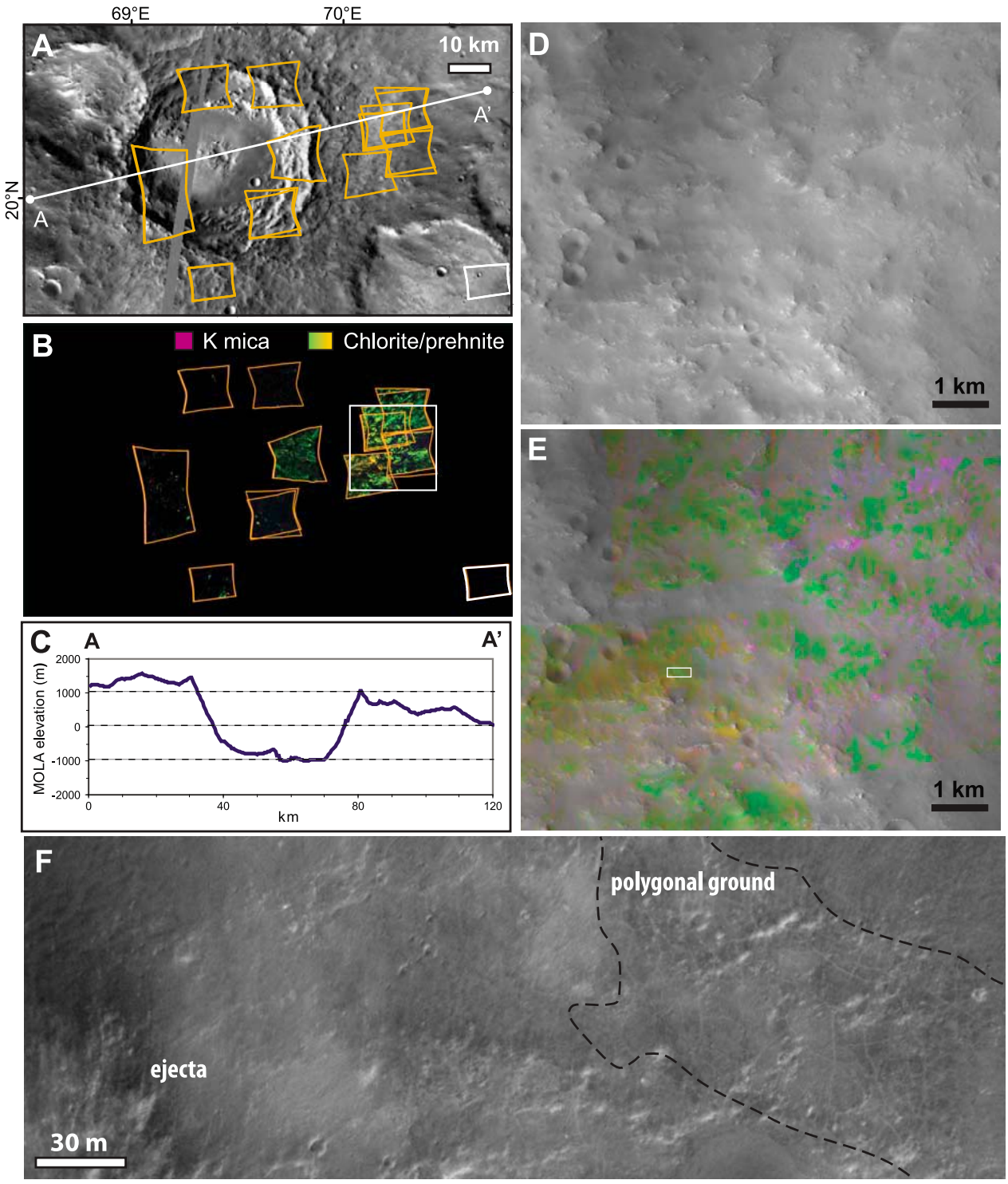

Figure 21. Distribution of chlorite/prehnite- and K mica–bearing materials around a 50 km impact crater near 20°N, 69°E. (a) THEMIS daytime infrared mosaic with outlines of CRISM images. (b) CRISM mineral maps (red, BD2350; green, D2300; blue, BD2200) in which K mica–bearing materials are magenta and chlorite/prehnite-bearing materials are green to yellow (as explained in section 4.2, these minerals are difficult to distinguish). Yellow indicates a more prominent 2.35-μm absorption. Some Fe/Mg smectites also present in the scene map as green; however, analysis of individual spectra show this phase is uncommon. (c) MOLA elevation profile across line A–A′ in Figure 21a. (d) Subset of CTX image P04_002651_1999_XI_19N289W_070219 from the box in Figure 21b. (e) Mineral indicators as in Figure 21b overlain on Figure 21d from CRISM images HRS00002FC5, FRT0000454E, FRT0000AACE, FRT0000A63F, and FRT0000B2C7. (f) Chlorite/prehnite-bearing ejecta and polygonal ground from northeast of a small crater taken from the location shown by the white box in Figure 21e.

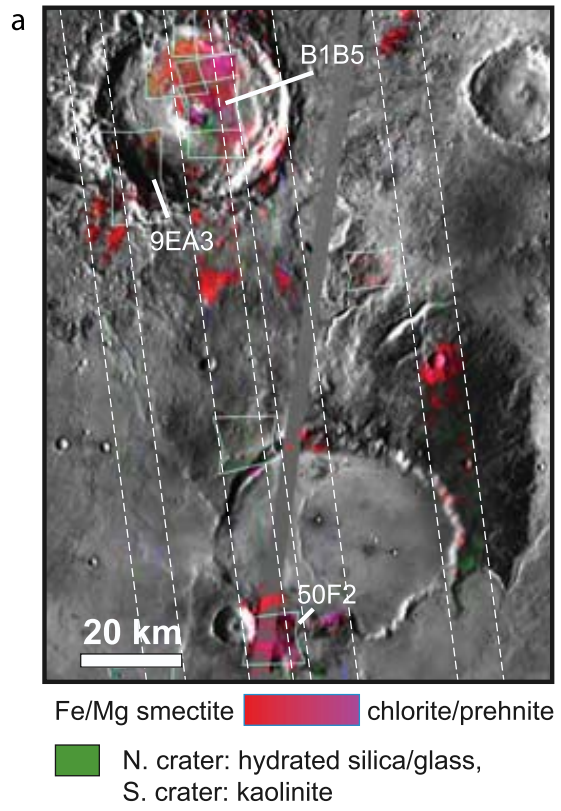

heavily eroded on one side. MOLA data show the eastern side is nearly 1 km lower than the western side (Figure 21c). CRISM images have been acquired of the crater's wallrock and ejecta. All scenes display some evidence for hydrated silicates (Figure 21b). Whereas the wall rocks contain phyllosilicates in only small, isolated knobs, spectral signatures of alteration minerals are found over nearly the entire surface in scenes acquired along the eastern wall and in terrains further east. Prehnite and chlorite (454E, Figure 5b) are the dominant minerals, displayed as green to yellow, yellow indicates a more prominent 2.35-μm absorption, in Figures 21d–21e. As discussed in section 4.2, these two minerals are difficult to distinguish in VNIR data. The prehnite/chlorite appears to originate from rocky knobs and small impact craters and is then dispersed by erosion. A few knobs have materials bearing the spectral signature of K mica (Figure 8) although these do not appear to be geomorphically distinct from prehnite/chlorite-bearing knobs (Figures 21d and 21e). Near some of the small craters, polygons with sides tens of meters in length have been observed, and these terrains are also chlorite/prehnite-bearing (Figure 21f).

[61] Immediately southwest of Nili Fossae, prehnite/chlorite occurs in wall rocks (e.g., 50F2, Figure 5b) and in the central peak materials of two 40 km impact craters (Figure 22), the northern of which has recently been named Toro crater by the International Astronomical Union. In their ejecta, Fe/Mg smectite is most common but chlorite/prehnite is found in a few small blocks. In Toro crater, small outcrops of hydrated silica (Figure 10) are found within the crater. A mélange of mixed hydrated silica, chlorite, and prehnite-bearing materials are found in the central peak, and the parameter maps as well as their spectra show these are mixed at 18 m/pixel CRISM resolution (Figure 22b). In contrast, no alteration minerals have been found in the interior of the southern crater, which has been covered by Syrtis Major lava flows. Around this crater's exterior are numerous small outcrops

Figure 22. (a) Craters in northern Syrtis Major (near 16°N, 72°E). THEMIS day infrared mosaic is shown with parameter maps (red, D2300; green, BD2200; blue, BD2350) from CRISM multispectral tile 1177 and FRT000050F2, FRT00009365, FRT00008D9A, HRL000086CA, FRT0000B1B5, HRL00009EA3, HRL0000B868, FRT00009786. White outlines show the coverage of the CRISM targeted (solid line) and mapping (dashed line) observations. Fe/Mg phyllosilicates present include Fe/Mg smectites (red) and chlorite (magenta). Prehnite (magenta) is also present and does not map distinctly from chlorite in this color mapping. Around the southern crater, kaolinite (green) is found. Within the northern crater (Toro), hydrated silica (green) is found. (b and c) The same color scheme is used for the targeted images FRT0000B1B5 and FRT000050F2 where the parameters are overlaid on a CRISM infrared albedo map. In the central peak of the northern crater in particular, there are mixed spectral phases (cyan, yellow) indicating chlorite, prehnite, hydrated silica, and possibly other hydrated phases spatially or intimately mixed in the same CRISM pixel. FRT000050F2 shows small craters exterior to the southern crater have associated Fe/Mg smectite, prehnite/chlorite, and kaolinite.

bearing kaolinite. Small craters that postdate the larger 40 km crater expose Fe/Mg smectites and chlorite in their walls and ejecta (Figure 22c).

6. Discussion

[62] The diversity of alteration minerals and, moreover, their distinctive associations and geomorphic expressions suggests that the nature of aqueous activity varied in space and time across the greater Nili Fossae region. After briefly discussing possible scenarios for formation of the Fe/Mg smectites, which are observed throughout the study area, we focus on key findings specific to the region: (1) in and around the Nili Fossae, evidence for multiple episodes of aqueous activity with neutral to alkaline waters during the period from the early Noachian to the late Hesperian and (2) in cratered terrains, evidence for low-temperature metamorphic or hydrothermal aqueous alteration. We then discuss some important outstanding questions that could form the basis for future work.

6.1. Widespread Fe/Mg Smectites

[63] As is the case planetwide, the high-resolution view provided by CRISM targeted images at Nili Fossae has greatly expanded the number of terrains known to contain Fe/Mg smectite [*Mustard et al.*, 2008]. In the greater Nili Fossae region, Fe/Mg smectites are found in bedrock as the lowermost stratigraphic unit in images sampling over 100,000 km^2. The spatial extent of the Fe/Mg smectite seems to exclude local lacustrine or volcanic hydrothermal processes as the primary formation mechanism. Rather for such widespread distribution, a more widespread process such as pedogenic leaching during alteration at the surface or subsurface hydrothermal activity related to crustal cooling or impacts is required. The brecciated nature of much of the smectite-bearing crust suggests the primacy of the role of impacts in distributing Fe/Mg smectites, if not also in creating them.

[64] Had there been insufficient time for reaction kinetics to produce thermodynamically favored phyllosilicate products, amorphous weathering products (e.g., allophane, palagonite, or their precursors) would be found rather than the spectrally distinct phyllosilicates that we observe. Hence, on the basis of terrestrial analogs, the materials in the Fe/Mg smectite-rich basement probably altered over at least thousands of years [*Eberl*, 1984; *Price et al.*, 2005], although the quantitative abundance of Fe/Mg smectite constituents relative to unaltered parent materials is an important additional constraint on the duration of aqueous activity. Estimates at Nili Fossae from phyllosilicate-bearing terrains are 20–35% phyllosilicate, a calculation that encompasses both abundance in bedrock and any covering sand or dust [*Poulet et al.*, 2008]. Nontronite and saponite typically form at low temperatures (<200°C) but can form and persist, i.e., not undergo transformation to other minerals, at temperatures up to 600°C under the right fluid chemistries so their thermal stability does not by itself constrain the likely formation environment [*Meunier*, 2005]. The partially altered Fe/Mg smectite–bearing brecciated rock unit that comprises the >600 m thick basement unit exposed by the Nili Fossae is representative of deep phyllosilicates of the early Noachian crust [*Mustard et al.*, 2009; *Murchie et al.*, 2009a]. It is exposed by extensive erosion around the fossae, but exhumed only locally by impact craters farther to the south and west. The spatially widespread nature of this Fe/Mg smectite suggests long-lived (likely at least $\sim 10^3$ years), pervasive water-rock interaction that was a regionally or globally important process for altering the earliest Martian crust.

6.2. Multiple Episodes of Aqueous Activity Around Nili Fossae

[65] Although smectites can form in numerous environmental settings, their accompaniment by additional alteration minerals provides additional constraints on timing, temperature, pressure, and aqueous geochemistry during alteration. In fact, the Nili Fossae region shows evidence for three episodes of aqueous activity: (1) alteration forming Fe/Mg smectites, (2) alteration to form overlying kaolinite or magnesium carbonate, and (3) erosion of units bearing these alteration minerals by fluvial activity and sapping channel formation.

[66] The coherent stratigraphy of layered phyllosilicates, i.e., kaolinite or carbonate bedrock always overlying smectite, in the immediate vicinity of Nili Fossae would not have been preserved during excavation and ejecta emplacement from the formation of the Isidis basin. Hence, a constraint is provided on (2), the timing of the formation of kaolinite and magnesium carbonate in eastern Nili Fossae; it postdates the Isidis impact, which is dated at ~3.96 Ga or approximately mid-Noachian [*Werner*, 2005]. A control on the distribution of carbonate versus kaolinite appears to be parent rock composition. The eastern portion of Nili Fossae is the site of the largest exposure of olivine-rich rocks on Mars [e.g., *Hoefen et al.*, 2003; *Hamilton and Christensen*, 2005; *Poulet et al.*, 2007; *Koeppen and Hamilton*, 2008] (Figure 1). These precursor ultramafic rocks in eastern Nili Fossae have, in some places, partially altered to Mg carbonate [*Ehlmann et al.*, 2008a]. In areas near the western part of Nili Fossae, where olivine is not usually identified in NIR spectral data, kaolinite instead typically occupies the middle stratigraphic layer between the Fe/Mg smectite and a capping rock.

[67] To the best resolution of HiRISE (25 cm/pixel), the tens of meters thick kaolinite-bearing unit is not bedded as might result from sedimentary transport. This may indicate that the kaolinite formed in place by alteration of parent rocks just as the magnesium carbonate apparently formed in place by alteration of olivine-rich rocks [*Ehlmann et al.*, 2008a]. A plausible formation mechanism for a kaolinite layer overlying smectite deposits is pedogenic-type leaching of preexisting phyllosilicates, leading to loss of Ca, Mg, and Fe ions from Fe/Mg smectite and its transformation to kaolinite. For example, kaolin-bearing soils form from basalts in Hawaii under intermediate leaching conditions; smectites are found in drier areas with less throughput of water whereas gibbsite and iron oxides are found in wetter environments [*Bates*, 1962; *Eberl*, 1984]. Alternating wet-dry cycles with prolonged periods of aridity appear to promote halloysite development [*Ziegler et al.*, 2003] on basalt, even under conditions that thermodynamically favor smectite. At Nili Fossae, the kaolin-bearing weathered soil unit might have subsequently been covered by the caprock material that presently overlies it. Kaolinite can, however, also form hydrothermally via precipitation from fluids. If a

hot impact melt sheet or hot ejecta were emplaced on water-bearing smectite-rich rocks, circulation of hydrothermal fluids might lead to kaolinite formation in the zone along the contact between smectite and ejected Isidis materials, which may constitute the caprock. While the morphology and stratigraphy of the caprock unit is well characterized [*Mustard et al.*, 2009], its composition and method of emplacement have not yet been ascertained. From spectral data, we see no evidence for the high-temperature polymorphs dickite and nacrite, which can be distinguished spectrally from kaolinite; however, kaolinite can also form and persist at high temperatures [*Zotov et al.*, 1998; *Fialips et al.*, 2003]. As discussed in section 4.4, the spectral data are consistent with kaolinite, halloysite or a mixture of kaolinite and smectite (mixed layer clay or physical mixture) (Figure 7) any of which are consistent with kaolinite formed in pedogenic processes.

[68] Like kaolinite, magnesium carbonates also can form in both surface and subsurface environments. On Earth, magnesite is uncommon but where found in large deposits is typically formed in playa environments fed by ultramafic catchments, during near surface alteration of serpentinized rock bodies, or from hydrothermal or serpentinization reactions at elevated temperatures by fluids circulating through ultramafic rocks in the subsurface [*Moeller*, 1989]. If in fact the serpentine found in Nili Fossae is associated with olivine-carbonate rocks as suggested by the band position of the 2.32 μm absorption in some exposures of partially altered olivine (Figure 17), one of the latter two mechanisms involving serpentinization is favored. Additional images of serpentine and partially altered olivine deposits will be acquired to assess the relationship between the two minerals.

[69] Sapping channels and valleys [*Mangold et al.*, 2007] cut the layered phyllosilicates in Nili Fossae. For example, layered Fe/Mg smectite and kaolinite sediments are cut by a channel draining a crater (Figure 15), and fossae walls have also been significantly eroded by alluvial activity (e.g., Figure 17) [*Mustard et al.*, 2009]. *Mangold et al.* [2007] constrain the timing of this erosive, fluvial episode (3) to be Late Noachian to Hesperian, which effectively brackets the timing of the formation of the kaolinite and carbonate (2). In most locations, this last episode of aqueous activity did not result in formation of alteration materials in transported sediments or in source watersheds [*Mangold et al.*, 2007]. However, in a few places (e.g., Figures 11 and 17a), hydrated minerals are precipitated in channel systems associated with this activity. This deposit appears to be a mixture of hydrated silica with either a sulfate or zeolite.

[70] Collectively, the alteration minerals in Nili Fossae point to waters of neutral to alkaline pH, which contrasts with acidic pH conditions indicated in other locations and perhaps in later time periods [*Hurowitz and McLennan*, 2007]. Carbonate persists to the present, associated with Hesperian channel systems. This indicates that waters were probably not acidic or that acidic waters were not in contact with the carbonate-bearing rocks for very long because this would have dissolved the carbonate [*Ehlmann et al.*, 2008a]. In fact, carbonate is an important component of Fe/Mg smectite–bearing deltaic sediments within Jezero crater. The similar layering of clays, Al-rich phyllosilicates over Fe/Mg smectite, at multiple locations across Mars [e.g., *Bishop et al.*, 2008a; *McKeown et al.*, 2009; *Murchie et al.*, 2009a; Noe Dobrea et al., submitted manuscript, 2009] may indicate similar formational processes. However, unlike the kaolinite seen in Mawrth Vallis [*McKeown et al.*, 2009], in the layered clays at Nili Fossae there is no evidence for any additional associated phase such as hydrated silica that would broaden the absorption at 2.2 μm. Coprecipitation of amorphous silica and kaolinite occurs at low pH but is less common at mildly acidic to neutral pH [*Fialips et al.*, 2000]. The observation of kaolinite-bearing rocks apparently in direct contact with carbonate-bearing rocks in at least one location (Figure 16) also suggests that this kaolinite did not form under acidic conditions. Rocks in and around Nili Fossae thus likely preserve a record for multiple episodes of aqueous alteration of a neutral to alkaline character, different from many sites elsewhere on Mars.

6.3. Mineralogic Evidence for Low-Temperature Metamorphic or Hydrothermal Alteration

[71] In cratered terrain surrounding the fossae (Noachian etched plains (Nple) [*Greeley and Guest*, 1987]), the types of alteration minerals are distinctly different from those in the immediate vicinity of the fossae. Chlorite, prehnite, hydrated silica, and analcime do not occur in a coherent stratigraphy but rather are exposed in breccia blocks, isolated outcrops or in eroded debris. However, in spite of the lack of clear geologic context, some of these minerals, particularly when considering the mineral associations in which they are found, point to aqueous alteration that occurred at elevated temperatures in the subsurface.

[72] The 1.48 μm band indicating the existence of prehnite (Figure 5) in mixtures in numerous craters in Nili Fossae provides the clearest evidence for hydrothermal or low-temperature metamorphic activity. Prehnite forms only under a highly restricted set of conditions: temperatures of 200–350°C, pressure <3 kbar, and a low partial pressure of CO_2 (e.g., $X_{CO2} < 0.004$ at 1.5 kbar) [*Schiffman and Day*, 1999; *Robinson and Bevins*, 1999]. On Earth, it is typically found in association with pumpellyite and chlorite in low-temperature metamorphosed rocks or in amygdules precipitated in the vesicles of basalt. *Poulet et al.* [2008] have reported the presence of pumpellyite within this crater on the basis of results from spectral mixture modeling. The prehnite now exposed in the central peak of Toro crater in north Syrtis Major (Figure 22b) could not have formed in its current setting from waters in contact with the CO_2-rich atmosphere. Rather, it probably formed from aqueous alteration at elevated temperatures in the subsurface and was brought to the surface by the impact. An alternative, less plausible scenario is formation of prehnite postimpact during hydrothermal circulation of waters in the central peak, which were out of contact with the atmosphere, and then subsequent extensive erosion of the central peak to expose the prehnite. However, the existence of prehnite/chlorite in both the central peak and crater ejecta suggests it likely formed during subsurface alteration that predates the impact. As reported by Buczkowski et al. [manuscript in preparation, 2009], occurrences of prehnite associated with craters around the Argyre basin suggest that this process was not unique to Nili Fossae.

[73] The small K mica–bearing rock outcrops among prehnite- and chlorite-bearing ridges are puzzling geologi-

cally. Though it has been found elsewhere in the southern highlands [*Fraeman et al.*, 2009], so far, K mica in Nili Fossae is restricted to one 50 km crater (Figures 2 and 21). It is difficult to tell whether the K mica, chlorite, and prehnite-bearing rocks constitute the ejecta of the crater or whether the entire eastern side of the crater has been heavily eroded and the chlorite, prehnite, and muscovite/illite simply represent exposed bedrock. In either case, the eastern side of the crater is some 1 km lower than the western side so rocks from deeper in the crust are probably being sampled. On Earth, K micas, e.g., muscovite, can be primary in granitic terrains. However, on Mars where basalt is dominant, K mica more likely results from hydrothermal activity or diagenesis. A key diagenetic process forming illite on Earth is conversion of smectite to illite upon burial, a process that is time- and depth-dependent and usually begins at temperatures of 50–80°C [*Hower*, 1976]. Dioctahedral smectites are converted first to mixed layer illite-smectites and then to illite of various polytypes. Higher-grade metamorphic/hydrothermal activity can generate muscovite. For trioctahedral smectites, with increasing temperature the reaction proceeds as saponite to corrensite (intermediate chlorite-smectite) and to chlorite [*Merriman and Peacor*, 1999]. In weakly metamorphosed rocks and sediments with a high ferromagnesian component, e.g., Fe/Mg smectites, a chlorite-illite assemblage with chlorite dominating can occur and may explain the alteration minerals around the 50 km crater.

[74] In the far west of the study area, craters have associated analcime-bearing rocks and aeolian hydrated silica deposits. Analcime and hydrated silica can originate in weathering reactions or from hydrothermal activity, and zeolites have been suggested as a possible constituent of Mars dust [*Ruff*, 2004]. In particular, the most common environments for analcime are highly alkaline lake waters [*Eugster*, 1980], weathering of tephra [*Sheppard and Hay*, 2001], and hydrothermal circulation < ~200°C as has been extensively studied for Icelandic basalts and Massif Central in France [e.g., *Weisenberger and Selbekk*, 2008; *Robert and Goffe*, 1993]. No evidence for layered sediments, which might indicate one of the first two mechanisms, exists in the two 25 km craters near the Antoniadi basin. The craters have been intensively studied in both near-infrared and thermal wavelengths to determine the composition of rocks and aeolian materials. TES deconvolution results show the central peak spectral unit to be enriched in quartz (total, 7%), feldspar (9%), and sheet silicates/high Si glass (33%) and depleted in pyroxene (9%) relative to nearby Syrtis Major plains materials [*Bandfield et al.*, 2004]. CRISM detects analcime, hydrated silica, chlorite, and Fe/Mg smectite. A mineral assemblage of Fe/Mg-rich smectites or chlorites with accessory zeolite, silica, quartz, and K-feldspar results from hydrothermal alteration in terrestrial craters [e.g., *Allen et al.*, 1982; *Naumov*, 2005] and suggests a possible reinterpretation of the "granitoid" material in the work of *Bandfield* [2006] as hydrothermal in origin rather than igneous, as has been proposed for other TES-detected high-silica materials near Hellas [*Bandfield*, 2008]. The moderate TES-modeled abundances of quartz and K-feldspar and their association with CRISM-detected hydrated Si-OH bearing phases (e.g., hydrated silica), phyllosilicates, and zeolites are consistent with such a formation process. Quartz, K-spar, analcime, and amorphous silica can form as amgydules in vesicles. Upon erosion of these rocks, more resistant silica-rich phases may be left behind as an aeolian lag, explaining the association of hydrated silica with mobile materials.

[75] Variations in the temperature, water-rock ratio, and fluid chemistry of hydrothermal systems may be responsible for these distinctive mineral assemblages observed in craters west of the Isidis basin. In all cases, however, fairly low-temperature (<350°C) metamorphic and/or hydrothermal processes are indicated by the mineral phases so far observed.

6.4. Key Questions for Future Work

[76] The diversity of alteration minerals detected in the region around the Nili Fossae is the highest yet observed on Mars. Why is the diversity so great here? Is it simply a result of a single event, the Isidis impact, and aqueous alteration, e.g., hydrothermal, immediately following and related to basin formation? The original Isidis crater has been heavily modified by tectonism, erosion, and deposition to create the Isidis basin seen today, and it is not entirely clear how far into the original impact basin the Nili Fossae are found. The fossae likely correspond to a megaterrace formed between the inner and outer basin rings [*Mustard et al.*, 2007]. The brecciated Fe/Mg smectites in the lowermost stratigraphic layer are the impacted materials, and olivine rich rocks at the base of an otherwise mineralogically indistinct cap unit are likely the product of an impact melt sheet [*Mustard et al.*, 2009]. The minerals found in smaller craters west of the basin could, if directly related to the Isidis impact, have been generated during hydrothermal activity within and around the outer basin ring. This is plausible given computational models of hydrothermal cooling that indicate hydrothermal systems can endure for 10^3 years or longer with increasing duration for larger impacts [*Rathbun and Squyres*, 2002; *Abramov and Kring*, 2005]. However, the coherency over hundreds of km of the layered stratigraphy in the eastern part of the study region is less easily explained by impact-induced processes. Moreover, the timing of at least the latest fluvial activity definitively postdates opening of the fossae [*Mangold et al.*, 2007]. These both suggest that any hydrothermal processes that might have been related to the Isidis impact represent only one of several episodes of regional aqueous activity.

[77] In terms of understanding the extent and duration of alteration in various terrains, initial efforts [*Poulet et al.*, 2008] to calculate modal mineralogy in phyllosilicate-bearing terrains should be expanded. An essential part of this effort will be expanding the number of well-characterized minerals and rock samples in publicly available spectral libraries as well as making laboratory measurements to measure their optical constants.

[78] While the mineralogic evidence points to low-temperature metamorphic or hydrothermal processes south and west of Nili Fossae near craters, a key question is their timing. Did these processes predate or postdate the impact craters with which they are associated? Understanding this requires high-resolution models of impact cratering processes. Some models predict shock temperatures near central peaks would be too high for phyllosilicates or

Table A1. Full Image IDs, Locations, and Number of Pixels Used for the Numerators and Denominators of CRISM Spectra Shown in Figures 4–12[a]

Label in Figure	CRISM Image ID	Center Pixel/Pixels	Number of Pixels
Figure 4			
9312 c/m (numerator)	FRT00009312	X:337 Y:230	ROI, 104
9312 c/m (denominator)	FRT00009312	X:337 Y:230, X:334, Y:155	ROIs, 112
A053 r/g (numerator)	FRT0000A053	X:457 Y:36	ROI, 94
A053 r/g (denominator)	FRT0000A053	X:457 Y:141	ROI, 71
9D44 c/m (numerator)	FRT00009D44	X:207 Y:181	ROI, 116
9D44 c/m (denominator)	FRT00009D44	X:207 Y:181	ROI, 99
3E12 r/g (numerator)	FRT00003E12	X:127 Y:397	ROI, 295
3E12 r/g (denominator)	FRT00003E12	X:127 Y:198	ROI, 386
A053 b/y (numerator)	FRT0000A053	X:274 Y:78	ROI, 205
A053 b/y (denominator)	FRT0000A053	X:274 Y:154, X:264 Y:170	ROIs, 176
9D44 r/g (numerator)	FRT00009D44	X:561 Y:143	ROI, 28
9D44 r/g (denominator)	FRT00009D44	X:561 Y:425	ROI, 19
64D9 r/g (numerator)	FRT000064D9	X:459 Y:7	ROI, 44
64D9 r/g (denominator)	FRT000064D9	X:459 Y:25	ROI, 28
527D r/g (numerator)	FRT0000527D	X:88 Y:103	ROI, 46
527D r/g (denominator)	FRT0000527D	X:88 Y:252	ROI, 81
50F2 c/m (numerator)	FRT000050F2	X:74 Y: 361	ROI, 1419
50F2 c/m (denominator)	FRT000050F2	X:74 Y: 294	ROI, 1172
Figure 5			
50F2 s1a	FRT000050F2	X:125 Y:434	5 × 5
50F2 s2a	FRT000050F2	X:125 Y:310	5 × 5
50F2 s1b	FRT000050F2	X: 216 Y:66, X:283 Y:82	5 × 5 + 5 × 5
50F2 s2b	FRT000050F2	X: 216 Y:177, X:283 Y:12	5 × 5 + 5 × 5
454E s1	FRT0000454E	X:243 Y:382	5 × 5
454E s2	FRT0000454E	X:243 Y:26	5 × 5
Figure 6			
ABCB s1	FRT0000ABCB	X:253 Y:60	5 × 3
ABCB s1	FRT0000ABCB	X:253 Y:15	5 × 3
B8C2 s1	HRL0000B8C2	X: 70 Y: 174	7 × 7
B8C2 s2	HRL0000B8C2	X: 70 Y: 59	7 × 7
Figure 7			
ABCB s1	FRT0000ABCB	X:387 Y:222	3 × 3
ABCB s2	FRT0000ABCB	X:387 Y:338	3 × 3
Figure 8			
2FC5 s1	HRS00002FC5	X:81 Y:14	2 × 2
2FC5 s2	HRS00002FC5	X:81 Y:53	2 × 2
454E s1	FRT0000454E	X:100 Y:405	5 × 5
454E s2	FRT0000454E	X:100 Y:373	5 × 5
Figure 9			
9312 s1	FRT00009312	X:174 Y:400	3 × 3
9312 s2	FRT00009312	X:174 Y:291	3 × 3
Figure 10			
9312 s1	FRT00009312	X:154 Y:170	11 × 11
9312 s2	FRT00009312	X:154 Y:370	11 × 11
9EA3 s1	HRL00009EA3	X:157 Y:359	ROI, 71
9EA3 s2	HRL00009EA3	X:156 Y:370	ROI, 79
Figure 11			
A4FC s1	FRT0000A4FC	X:191 Y:122, X:113 Y:211, X:61 Y:187	ROIs, 136
A4FC s2	FRT0000A4FC	X:191 Y:134, X:113 Y:178, X:61 Y:375	ROIs, 144
Figure 12			
A09C s1	FRT0000A09C	X:50 Y:98	ROIs, 277
A09C s2	FRT0000A09C	X:50 Y:186	ROIs, 522
40FF s1	HRL000040FF	X:42 Y:347, X:186 Y:367, X:263 Y:296	ROIs, 1425
40FF s2	HRL000040FF	X:76 Y:238, X:85 Y:76, X:237 Y:22, X:263 Y:91	ROIs, 5277

[a]All pixel locations are given for unprojected CRISM image data.

silicate hydroxides to survive [*Marzo et al.*, 2008; *Fairen et al.*, 2008]; others have lower initial temperatures [*Barnhart et al.*, 2008]. The ability to model discrete packets of materials within the preimpact surface and their movement and temperature throughout compaction and compression, excavation, and adjustment stages is key to understanding the degree of heterogeneity of temperatures experienced by impacted materials as well as where they end up after the most intense period of the modification stage. This would allow understanding the likely distribution and thermal history of impacted subsurface units. Also important will be moving beyond which minerals are thermodynamically stable to understanding the kinetic rates for formation and destruction of alteration minerals [*Schwenzer and Kring*, 2009]. By coupling detailed knowledge of temperature and mass movement with understanding of the rates of mineral formation/destruction, the question of preimpact or postimpact alteration can be rigorously assessed. Also important will be advances in interpretation of VNIR spectra, in particular of mixed layer

Table A2. Source and Full Sample Identifier for the Laboratory Library Spectra Shown in Figures 4–12

Label in Figure	Source	Source Sample ID	Notes
Figure 4			
Fe-smectite SWa-1	*Clark et al.* [2007]	Nontronite SWa-1.a	
Nontronite NG-1	*Clark et al.* [2007]	Nontronite NG-1.a	
Hectorite SHCa-1	*Clark et al.* [2007]	Hectorite SHCa-1	
Sepiolite SepNev-1	*Clark et al.* [2007]	Sepiolite SepNev-1	
Saponite SapCa-1	*Clark et al.* [2007]	Saponite SapCa-1	
Figure 5			
Prehnite	*Clark et al.* [2007]	Prehnite GDS613.a < 60 um	
Pumpellyite, Ca-rich	RELAB	ZE-EAC-001-c1ze01	sample descriptions by E. Cloutis[a]
Pumpellyite, Mg-rich	RELAB	ZE-EAC-002-c1ze02	sample descriptions by E. Cloutis[a]
Chlorite	*Clark et al.* [2007]	chlorite_smr13.4984	
Clinochlore (Fe:Mg 0.57)	*Clark et al.* [2007]	clinochlore_gds158.5327	
Clinochlore (Fe:Mg 1.5)	*Clark et al.* [2007]	clinochlore_gds157.5542	
Figure 6			
Antigorite	*Clark et al.* [2007]	Antigorite NMNH96917.b 165u	
Lizardite	*Clark et al.* [2007]	Lizardite NMHR4687	
Saponite	*Clark et al.* [2007]	Saponite SapCa-1	
Figure 7			
Montmorillonite	*Clark et al.* [2007]	Montmorillonite SWy-1	
Kaol-smect	*Clark et al.* [2007]	kaolsmect_h89fr2.25636	
Kaolinite, wxl	*Clark et al.* [2007]	kaolinite_kga1.12117	
Kaolinite, pxl	*Clark et al.* [2007]	kaolinite_pfn1_kga2.12176	
Halloysite	*Clark et al.* [2007]	halloysite_nmnh106236.8988	
Nacrite	*Clark et al.* [2007]	Nacrite GDS88	
Dickite	*Clark et al.* [2007]	Dickite NMNH106242	
Figure 8			
Muscovite	*Clark et al.* [2007]	Muscovite GDS116 Tanzania	
Muscovite (hydrated)	*Clark et al.* [2007]	Muscovite GDS111 Guatemal	
Illite, 2M, hydT	*Clark et al.* [2007]	Illite IL101 (2M2)	see also *Kruse and Hauff* [1991]
Illite, 2M, sed.	*Clark et al.* [2007]	Illite GDS4 (Marblehead)	see also *Kruse and Hauff* [1991]
Illite, 1M, sed.	*Clark et al.* [2007]	Illite IMt-1.a	see also *Kruse and Hauff* [1991]
Illite, 1M, disordered	*Clark et al.* [2007]	Illite IL105 (1Md)	see also *Kruse and Hauff* [1991]
Figure 9			
Analcime	*Clark et al.* [2007]	Analcime GDS1 Zeolite	
Stilbite	*Clark et al.* [2007]	Stilbite GDS8 Zeolite	
Mordenite	*Clark et al.* [2007]	Mordenite GDS18	
Natrolite	*Clark et al.* [2007]	Natrolite HS169.3B Zeolite	
Figure 10			
Hydrated basaltic glass	G. Swayze (personal communication, 2008)	Hydrated Basaltic Glass MLUT03–9C 7torr 240 K 45 min	shown at 10X actual reflectance
Opal A/CT mixture	*Clark et al.* [2007]	Opal TM8896 (Hyalite)	
Figure 11			
Opal	*Clark et al.* [2007]	Opal TM8896 (Hyalite)	
Chalcedony	*Clark et al.* [2007]	Chalcedony CU91–6A	
Chabazite	RELAB	Zeolite Chabazite ZE-EAC-017 LAZE17	sample descriptions by E. Cloutis[a]
Heulandite	RELAB	Zeolite Heulandite ZE-EAC-031LAZE31	sample descriptions by E. Cloutis[a]
Thomsonite	RELAB	Zeolite Thomsonite ZE-EAC-009LAZE09	sample descriptions by E. Cloutis[a]
Mg sulfate	RELAB	Magnesium Sulfate JB-JLB-366- 799F366	
Fe sulfate	RELAB	Copiapite CC-JFM-013-A- F1CC13A	
Figure 12			
Magnesite CB-EAC-006A	RELAB	CB-EAC-006A-lacb06a	sample descriptions by E. Cloutis[a]
Magnesite CC-JFM-006B	RELAB	CC-JFM-006B-f1cc06b	
Siderite	*Clark et al.* [2007]	Siderite HS271.3B	
Coalingite	RELAB	CB-EAC-023-A-lacb23a	sample descriptions by E. Cloutis[a]
Mg carb. (hydromag.)	RELAB	JB-JLB-590-bkr1jb590	
Magnesite + Hydromag.	*Clark et al.* [2007]	Magnesite + Hydroma HS47.3B	
Lizardite	*Clark et al.* [2007]	Lizardite NMNHR4687.b 165	
Nontronite	*Clark et al.* [2007]	Nontronite NG-1.a	
Brucite	*Clark et al.* [2007]	Brucite HS34827.3B	

[a]Available at psf.uwinnipeg.ca/Sample_Database.html.

clays such as illite-smectite and smectite-chlorite, in order to distinguish the degree of diagenesis/metamorphism.

[79] As CRISM continues to map the surface of Mars, the uniqueness of the mineralogic diversity found in the Nili Fossae region will be assessed. Further efforts will also examine the S detector data to look for evidence of aqueous alteration provided by iron oxide minerals. Was the region around the Nili Fossae unusually wet in comparison to other regions of Mars? How much of the Noachian megabreccia [*McEwen et al.*, 2008] of Mars is altered? Already, some of the alteration minerals (e.g., K mica, hydrated silica, chlorite) have been found elsewhere in the southern highlands, associated with craters in the Terra Tyrrhena region [*Fraeman et al.*, 2009]. Diverse alteration minerals have

been mapped first in the well-exposed Nili Fossae region, following up on regional-scale OMEGA phyllosilicate detections; however, with future exploration, we may find aqueous activity, including low-grade metamorphic or hydrothermal activity, was much more widespread on ancient Mars than previously known.

7. Conclusions

[80] In the Noachian terrain west of the Isidis basin, alteration minerals identified by CRISM based on distinctive absorptions from 1.0 to 2.6 μm include nontronite and magnesium smectites, chlorite, prehnite, serpentine, kaolinite, K mica, analcime, hydrated silica, and magnesium carbonate. While Fe/Mg smectites are found throughout the study area over a much greater area than previously known, the distribution of the other discovered alteration minerals is not homogeneous. Rather, these tend to occur in provinces with distinctive assemblages of alteration minerals and geomorphic settings.

[81] Stratigraphic relationships among units bearing alteration minerals can be discerned in the eastern part of the study area, in eroded terrains in and around the Nili Fossae, where layered clays with Fe/Mg smectite, Mg carbonate, and kaolinite are found. In bedrock units, Mg carbonate and kaolinite occur above Fe/Mg smectite–bearing units. Magnesium carbonate is more common near the eastern Nili Fossae and kaolinite is more common in the west. This probably reflects the nature of the parent material, namely the prevalence of more olivine-rich rocks in the east that can alter to magnesium carbonate.

[82] In and around impact craters west and south of the Nili Fossae, illite, analcime, and prehnite serve as mineralogic indicators for alteration at elevated temperatures in the subsurface. Low-temperature metamorphism or hydrothermal activity is most definitively indicated by prehnite where alteration occurred out of contact with the CO_2 atmosphere and at temperatures between 200 and 350°C. While Fe/Mg smectite is still found associated with these impact craters, chlorite- and prehnite-bearing materials are much more common in the cratered terrains west and south of the Nili Fossae and may reflect conversion of smectites to chlorite by burial and/or exposure to higher temperatures at depth.

[83] Key questions for future work include constraining whether aqueous alteration at elevated temperature predated or postdated impact structures and more definitively constraining the environment of carbonate and kaolinite formation. Regardless, the mineralogic diversity of the region around the Nili Fossae indicates multiple episodes of aqueous activity in multiple distinct environments. An initial phase of Fe/Mg smectite formation in the early to mid-Noachian was apparently followed by episodes of subsurface or surface aqueous mineralogic alteration, culminating finally in Hesperian fluvial reworking that led to little mineralogic alteration. The resultant alteration minerals at Nili Fossae are more typical of those resulting from neutral to alkaline conditions rather than acidic conditions thought to have dominated other regions of Mars. The excellent exposure of bedrock units and the apparently long and complex history of aqueous activity in the region around the Nili Fossae make this part of Mars a compelling destination for future in situ investigations.

Appendix A

[84] Using the processing steps outlined in section 3, other users of CRISM data can replicate the spectral data shown herein using information provided in this appendix. The image number, coordinates of the center point of spectral data, and size of the region of interest are given for all CRISM spectral data shown in Figures 4–12 (Table A1). Information on the mineral samples whose library spectra were used for identification of mineral phases on Mars is given in Table A2.

[85] **Acknowledgments.** Mario Parente and Frank Seelos provided numerous useful suggestions on data analysis for this manuscript. Thanks to Lynn Carlson, Nicolas Mangold, and Nancy McKeown for helpful advice on techniques for combining data sets to make geologic interpretations. We appreciate the many helpful discussions with members of the CRISM team and the ongoing, dedicated efforts of the CRISM-SOC to acquire this spectacular data set. Reviewers Brad Dalton and Victoria Hamilton provided detailed comments that improved this manuscript. We also thank the CTX and HiRISE teams for their commitment to coordinated observations which enable high-resolution studies of Mars mineralogy with morphology.

References

Abramov, O., and D. A. Kring (2005), Impact-induced hydrothermal activity on early Mars, *J. Geophys. Res.*, *110*, E12S09, doi:10.1029/2005JE002453.

Allen, C. C., J. L. Gooding, and K. Keil (1982), Hydrothermally altered impact melt rock and breccia: Contributions to the soil of Mars, *J. Geophys. Res.*, *87*, 10,083–10,101, doi:10.1029/JB087iB12p10083.

Anderson, J. H., Jr., and K. A. Wickersheim (1964), Near infrared characterization of water and hydroxyl groups on silica surfaces, *Surf. Sci.*, *2*, 252–260, doi:10.1016/0039-6028(64)90064-0.

Arvidson, R. E., et al. (2006), Nature and origin of the hematite-bearing plains of Terra Meridiani based on analyses of orbital and Mars Exploration rover data sets, *J. Geophys. Res.*, *111*, E12S08, doi:10.1029/2006JE002728.

Bandfield, J. L. (2006), Extended surface exposures of granitoid compositions in Syrtis Major, Mars, *Geophys. Res. Lett.*, *33*, L06203, doi:10.1029/2005GL025559.

Bandfield, J. L. (2008), High-silica deposits of an aqueous origin in western Hellas Basin, Mars, *Geophys. Res. Lett.*, *35*, L12205, doi:10.1029/2008GL033807.

Bandfield, J. L., V. E. Hamilton, P. R. Christensen, and H. Y. McSween Jr. (2004), Identification of quartzofeldspathic materials on Mars, *J. Geophys. Res.*, *109*, E10009, doi:10.1029/2004JE002290.

Barnhart, C. J., F. Nimmo, and B. J. Travis (2008), Geophysical controls on Martian post-impact hydrothermal systems, *Lunar Planet. Sci.*, *XXXIX*, Abstract 2294.

Bates, T. F. (1962), Halloysite and gibbsite formation in Hawaii, *Clays Clay Miner.*, *9*, 315–328, doi:10.1346/CCMN.1960.0090119.

Bibring, J.-P., et al. (2005), Mars surface diversity as revealed by the OMEGA/Mars Express observations, *Science*, *307*, 1576–1581, doi:10.1126/science.1108806.

Bibring, J.-P., et al. (2006), Global mineralogical and aqueous Mars history derived from OMEGA/Mars Express data, *Science*, *312*, 400–404, doi:10.1126/science.1122659.

Bishop, J. L., C. M. Pieters, and J. O. Edwards (1994), Infrared spectroscopic analyses on the nature of water in montmorillonite, *Clays Clay Miner.*, *42*, 702–716, doi:10.1346/CCMN.1994.0420606.

Bishop, J., J. Madejova, P. Komadel, and H. Froschl (2002a), The influence of structural Fe, Al, and Mg on the infrared OH bands in spectra of dioctahedral smectites, *Clay Miner.*, *37*, 607–616, doi:10.1180/0009855023740063.

Bishop, J. L., E. Murad, and M. D. Dyar (2002b), The influence of octahedral and tetrahedral cation substitution on the structure of smectites and serpentines as observed through infrared spectroscopy, *Clay Miner.*, *37*, 617–628, doi:10.1180/0009855023740064.

Bishop, J. L., et al. (2008a), Phyllosilicate diversity and past aqueous activity revealed at Mawrth Vallis, Mars, *Science*, *321*, 830–833, doi:10.1126/science.1159699.

Bishop, J. L., M. D. Lane, M. D. Dyar, and A. J. Brown (2008b), Reflectance and emission spectroscopy of four groups of phyllosilicates: Smectites, kaolinite-serpentines, chlorites, and micas, *Clay Miner.*, *43*, 35–54, doi:10.1180/claymin.2008.043.1.03.

Calvin, W. M., and T. V. V. King (1997), Spectral characteristics of iron-bearing phyllosilicates: Comparison to Orgueil (CI1), Murchinson, and Murray (CM2), *Meteorit. Planet. Sci.*, *32*, 693–701.

Calvin, W. M., T. V. V. King, and R. N. Clark (1994), Hydrous carbonates on Mars?: Evidence from Mariner 6/7 infrared spectrometer and ground-based telescopic spectra, *J. Geophys. Res.*, *99*, 14,659–14,675, doi:10.1029/94JE01090.

Chevrier, V., F. Poulet, and J.-P. Bibring (2007), Early geochemical environment of Mars as determined from thermodynamics of phyllosilicates, *Nature*, *448*, 60–63, doi:10.1038/nature05961.

Christensen, P. R., et al. (2004), The Thermal Emission Imaging System (THEMIS) for the Mars 2001 Odyssey mission, *Space Sci. Rev.*, *110*, 85–130, doi:10.1023/B:SPAC.0000021008.16305.94.

Clark, R. N., and T. M. Hoefen (2000), Spectral feature mapping with Mars Global Surveyor Thermal Emission Spectra: Mineralogic implications, *Bull. Am. Astron. Soc.*, *32*, 1118.

Clark, R. N., T. V. V. King, M. Klejwa, G. A. Swayze, and N. Vergo (1990a), High spectral resolution reflectance spectroscopy of minerals, *J. Geophys. Res.*, *95*, 12,653–12,680, doi:10.1029/JB095iB08p12653.

Clark, R. N., G. A. Swayze, R. B. Singer, and J. B. Pollack (1990b), High-resolution reflectance spectra of Mars in the 2.3- μm region: Evidence for the mineral scapolite, *J. Geophys. Res.*, *95*, 14,463–14,480, doi:10.1029/JB095iB09p14463.

Clark, R. N., G. A. Swayze, R. Wise, K. E. Livo, T. M. Hoefen, R. F. Kokaly, and S. J. Sutley (2007), USGS Digital Spectral Library splib06a, *U.S. Geol. Surv. Data*, 231.

Clark, R. N., et al. (2008), Diversity of mineralogy and occurrences of phyllosilicates on Mars, *Eos Trans. AGU*, *89*(53), Fall Meet. Suppl., Abstract P43D–04.

Cloutis, E. A., P. M. Asher, and S. A. Mertzman (2002), Spectral reflectance properties of zeolites and remote sensing implications, *J. Geophys. Res.*, *107*(E9), 5067, doi:10.1029/2000JE001467.

Cloutis, E. A., et al. (2006), Detection and discrimination of sulfate minerals using reflectance spectroscopy, *Icarus*, *184*, 121–157, doi:10.1016/j.icarus.2006.04.003.

Crowley, J. K., and N. Vergo (1988), Near-infrared reflectance spectra of mixtures of kaolin-group minerals: Use in clay mineral studies, *Clays Clay Miner.*, *36*, 310–316, doi:10.1346/CCMN.1988.0360404.

Eberl, D. D. (1984), Clay mineral formation in rocks and soils, *Philos. Trans. R. Soc. London, Ser. A*, *311*, 241–257, doi:10.1098/rsta.1984.0026.

Ehlmann, B. L., et al. (2008a), Orbital identification of carbonate-bearing rocks on Mars, *Science*, *322*, 1828–1832, doi:10.1126/science.1164759.

Ehlmann, B. L., et al. (2008b), Clay minerals in delta deposits and organic preservation potential on Mars, *Nat. Geosci.*, *1*, 355–358, doi:10.1038/ngeo207.

Eugster, H. P. (1980), Geochemistry of evaporitic lacustrine deposits, *Annu. Rev. Earth Planet. Sci.*, *8*, 35–63, doi:10.1146/annurev.ea.08.050180.000343.

Fairen, A. G., A. F. Davila, G. A. Marzo, T. L. Roush, and C. P. McKay (2008), Post-Noachian water activity on Mars inferred from shock decomposition analysis of phyllosilicates within impact craters, paper presented at Workshop on Martian Phyllosilicates, Abstract 7021, Cent. Natl. d'Etud. Spatiales, 21–23 Oct., Paris.

Fassett, C. I., and J. W. Head III (2005), Fluvial sedimentary deposits on Mars: Ancient deltas in a crater lake in the Nili Fossae region, *Geophys. Res. Lett.*, *32*, L14201, doi:10.1029/2005GL023456.

Fialips, C.-I., S. Petit, A. Decarreau, and D. Beaufort (2000), Influence of synthesis pH on kaolinite "crystallinity" and surface properties, *Clays Clay Miner.*, *48*, 173–184, doi:10.1346/CCMN.2000.0480203.

Fialips, C.-I., J. Majzlan, D. Beaufort, and A. Navrotsky (2003), New thermochemical evidence on the stability of dickite vs. kaolinite, *Am. Mineral.*, *88*, 837–845.

Fraeman, A. A., et al. (2009), Evaluating models of crustal cooling using CRISM observations of impact craters in Terra Tyrrhena and Noachis Terra, *Lunar Planet. Sci.*, *XL*, Abstract 2320.

Frey, M., and D. Robinson (Eds.) (1999), *Low-Grade Metamorphism*, 313 pp., Blackwell Sci, Oxford, U. K.

Frost, R. L., J. T. Kloprogge, and Z. Ding (2002), Near-infrared spectroscopic study of nontronites and ferruginous smectite, *Spectrochim. Acta Part A*, 1657–1668.

Gaffey, S. J. (1987), Spectral reflectance of carbonate minerals in the visible and near infrared (0.35–2.55 um): Anhydrous carbonate minerals, *J. Geophys. Res.*, *92*, 1429–1440, doi:10.1029/JB092iB02p01429.

Gendrin, A., et al. (2005), Sulfates in Martian layered terrains: The OMEGA/Mars Express view, *Science*, *307*, 1587–1591, doi:10.1126/science.1109087.

Giese, R. F. (1988), Kaolin minerals: Structures and stabilities, in *Reviews in Mineralogy*, vol. 19, *Hydrous Phyllosilicates (Exclusive of Micas)*, edited by S. W. Bailey, pp. 29–62, Mineral. Soc. of Am., Washington, D. C.

Goryniuk, M. C., B. A. Rivard, and B. Jones (2004), The reflectance spectra of opal-A (0.5–25 um) from the Taupo Volcanic Zone: Spectra that may identify hydrothermal systems on planetary surfaces, *Geophys. Res. Lett.*, *31*, L24701, doi:10.1029/2004GL021481.

Grant, J. A., et al. (2008), HiRISE imaging of impact megabreccia and submeter aqueous strata in Holden Crater, Mars, *Geology*, *36*, 195–198, doi:10.1130/G24340A.1.

Grauby, O., S. Petit, A. Decarreau, and A. Baronnet (1994), The nontronite-saponite series: An experimental approach, *Eur. J. Mineral.*, *6*, 99–112.

Greeley, R., and J. E. Guest (1987), Geologic map of the eastern equatorial region of Mars, *U.S. Geol. Surv. Misc. Invest. Ser. Map I-1802-B*.

Hamilton, V. E., and P. R. Christensen (2005), Evidence for extensive, olivine-rich bedrock on Mars, *Geology*, *33*, 433–436, doi:10.1130/G21258.1.

Hamilton, V. E., P. R. Christensen, H. Y. McSween Jr., and J. L. Bandfield (2003), Searching for the source regions of Martian meteorites using MGS TES: Integrating Martian meteorites into the global distribution of igneous materials on Mars, *Meteorit. Planet. Sci.*, *38*(6), 871–885.

Hartmann, W. K., and G. Neukum (2001), Cratering chronology and the evolution of Mars, *Space Sci. Rev.*, *96*, 165–194, doi:10.1023/A:1011945222010.

Haskin, L. A., et al. (2005), Water alteration of rocks and soils on Mars at the Spirit rover site in Gusev crater, *Nature*, *436*, 66–69, doi:10.1038/nature03640.

Hay, R. L. (1986), Geologic occurrence of zeolites and some associated minerals, *Pure Appl. Chem.*, *58*(10), 1339–1342, doi:10.1351/pac198658101339.

Hoefen, T. M., R. N. Clark, J. L. Bandfield, M. D. Smith, J. C. Pearl, and P. R. Christensen (2003), Discovery of olivine in the Nili Fossae region of Mars, *Science*, *302*, 627–630, doi:10.1126/science.1089647.

Hower, J. (1976), Mechanism of burial metamorphism of argillaceous sediment: 1. Mineralogical and chemical evidence, *Geol. Soc. Am. Bull.*, *87*(5), 725–737, doi:10.1130/0016-7606(1976)87<725:MOBMOA>2.0.CO;2.

Hunt, G. R., and J. W. Salisbury (1971), Visible and near-infrared spectra of minerals and rocks: II. Carbonates, *Mod. Geol.*, *2*, 23–30.

Hunt, G. R., J. W. Salisubury, and C. J. Lenhoff (1973), Visible and near infrared spectra of minerals and rocks: VI. Additional silicates, *Mod. Geol.*, *4*, 85–106.

Hurowitz, J. A., and S. M. McLennan (2007), A 3.5 Ga record of water-limited, acidic weathering conditions on Mars, *Earth Planet. Sci. Lett.*, *260*, 432–443, doi:10.1016/j.epsl.2007.05.043.

King, T. V. V., and R. N. Clark (1989), Spectral characteristics of chlorites and Mg-serpentines using high resolution reflectance spectroscopy, *J. Geophys. Res.*, *94*, 13,997–14,008, doi:10.1029/JB094iB10p13997.

Koeppen, W. C., and V. E. Hamilton (2008), Global distribution, composition, and abundance of olivine on the surface of Mars from thermal infrared data, *J. Geophys. Res.*, *113*, E05001, doi:10.1029/2007JE002984.

Kruse, F. A., and P. L. Hauff (1991), Identification of illite polytype zoning in disseminated gold deposits using reflectance spectroscopy and X-ray diffraction: Potential for mapping with imaging spectrometers, *IEEE Trans. Geosci. Remote Sens.*, *29*(1), 101–104, doi:10.1109/36.103298.

Lane, M. D., and P. R. Christensen (1997), Thermal emission spectroscopy of anhydrous carbonates, *J. Geophys. Res.*, *102*, 25,581–25,592, doi:10.1029/97JE02046.

Langer, K., and O. W. Florke (1974), Near infrared absorption spectra (4000–9000 cm-1) of opals and the role of "water" in these SiO2*nH2O minerals, *Fortschr. Mineral.*, *52*, 17–51.

Line, C. M. B., A. Putnis, C. Putnis, and C. Giampaolo (1995), The dehydration kinetics and microtexture of analcime from two parageneses, *Am. Mineral.*, *80*, 268–279.

Lonker, S. W., and J. D. Fitzgerald (1990), Formation of coexisting 1M and 2M polytypes in illite from an active hydrothermal system, *Am. Mineral.*, *75*, 1282–1289.

Luhr, J. F., and T. K. Kyser (1989), Primary igneous analcime: The Colima minettes, *Am. Mineral.*, *74*, 216–223.

Malin, M. C., et al. (2007), Context Camera Investigation on board the Mars Reconnaissance Orbiter, *J. Geophys. Res.*, *112*, E05S04, doi:10.1029/2006JE002808.

Mangold, N., et al. (2007), Mineralogy of the Nili Fossae region with OMEGA/Mars Express data: 2. Aqueous alteration of the crust, *J. Geophys. Res.*, *112*, E08S04, doi:10.1029/2006JE002835.

Marzo, G. A., et al. (2008), Evidence for relatively recent hydrothermal activity due to an impact within the Syrtis Major, *Eos Trans. AGU*, *89*(53), Fall Meet. Suppl., Abstract P53A–1438.

McEwen, A. S., et al. (2007), Mars Reconnaissance Orbiter's High Resolution Imaging Science Experiment (HiRISE), *J. Geophys. Res.*, *112*, E05S02, doi:10.1029/2005JE002605.

McEwen, A. S., L. Tornabene, J. Grant, J. Wray, and J. Mustard (2008), Noachian megabreccia on Mars, *AGU*, *89*(53), Fall Meet. Suppl., Abstract P43D–03.

McKeown, N. K., et al. (2009), Characterization of phyllosilicates observed in the central Mawrth Vallis region, Mars, their potential formational processes, and implications for past climate, *J. Geophys. Res.*, doi:10.1029/2008JE003301, in press.

Merriman, R. J., and D. R. Peacor (1999), Very low-grade metapelites: Mineralogy, microfabrics, and measuring reaction progress, in *Low-Grade Metamorphism*, edited by M. Frey and D. Robinson, pp. 10–60, Blackwell Sci., Oxford, U. K.

Meunier, A. (2005), *Clays*, 472 pp., Springer, Berlin.

Milliken, R. E., and J. F. Mustard (2005), Quantifying absolute water content of minerals using near-infrared reflectance spectroscopy, *J. Geophys. Res.*, *110*, E12001, doi:10.1029/2005JE002534.

Milliken, R. E., et al. (2008), Opaline silica in young deposits on Mars, *Geology*, *36*, 847–850, doi:10.1130/G24967A.1.

Moeller, P. (Ed.) (1989), *Magnesite: Geology, Mineralogy, Geochemistry, Formation of Mg-Carbonates*, *Monogr. Ser. Miner. Deposits*, vol. 28, 300 pp., Gebrüder Borntraeger, Berlin.

Murchie, S. L., et al. (2007a), Compact Reconnaissance Imaging Spectrometer for Mars (CRISM) on Mars Reconnaissance Orbiter (MRO), *J. Geophys. Res.*, *112*, E05S03, doi:10.1029/2006JE002682.

Murchie, S., E. Guinness, and S. Slavney (2007b), CRISM data product software interface specification, ftp://pds-geosciences.wustl.edu/mro-crism/mro-m-crism-2-edr-v1/mrocr_0001/document/crism_dpsis.pdf, NASA Planet. Data Syst., Greenbelt, Md., 17 Aug.

Murchie, S. L., et al. (2009a), A synthesis of Martian aqueous mineralogy after one Mars year of observations from the Mars Reconnaissance Orbiter, *J. Geophys. Res., 114*, E00D06, doi:10.1029/2009JE003342.

Murchie, S. L., et al. (2009b), Compact Reconnaissance Imaging Spectrometer investigation and data set from the Mars Reconnaissance Orbiter's primary science phase, *J. Geophys. Res., 114*, E00D07, doi:10.1029/2009JE003344.

Murray, H. H. (1988), Kaolin minerals: Structures and stabilities, in *Reviews in Mineralogy*, vol. 19, *Hydrous Phyllosilicates (Exclusive of Micas)*, edited by S. W. Bailey, pp. 67–87, Mineral. Soc. of Am., Washington, D. C.

Mustard, J. F., et al. (2005), Olivine and pyroxene diversity in the crust of Mars, *Science*, *307*, 1594–1597, doi:10.1126/science.1109098.

Mustard, J. F., et al. (2007), Mineralogy of the Nili Fossae region with OMEGA/Mars Express data: 1. Ancient impact melt in the Isidis basin and implications for the transition from the Noachian to Hesperian, *J. Geophys. Res.*, *112*, E08S03, doi:10.1029/2006JE002834.

Mustard, J. F., et al. (2008), Hydrated silicate minerals on Mars observed by the CRISM instrument on MRO, *Nature*, *454*, 305–309, doi:10.1038/nature07097.

Mustard, J. F., et al. (2009), Composition, Morphology, and Stratigraphy of Noachian Crust around the Isidis basin, *J. Geophys. Res.*, doi:10.1029/2009JE003349, in press.

Naumov, M. V. (2005), Principal features of impact-generated hydrothermal circulation systems: Mineralogical and geochemical evidence, *Geofluids*, *5*(3), 165–184, doi:10.1111/j.1468-8123.2005.00092.x.

Nelson, M. J., H. E. Newsom, and D. S. Draper (2005), Incipient hydrothermal alteration of basalts and the origin of Martian soil, *Geochim. Cosmochim. Acta*, *69*, 2701–2711, doi:10.1016/j.gca.2005.01.020.

Newsom, H. E. (1980), Hydrothermal alteration of impact melt sheets with implications for Mars, *Icarus*, *44*, 207–216, doi:10.1016/0019-1035(80)90066-4.

Parente, M. (2008), A new approach to denoising CRISM images, *Lunar Planet. Sci.*, *XXXIX*, Abstract 2528.

Parmentier, E. M., J. F. Mustard, B. L. Ehlmann, and L. H. Roach (2008), Deep hydrothermal circulation and implications for the early crustal compositional and thermal evolution of Mars, *Lunar Planet. Sci.*, *XXXIX*, Abstract 1544.

Pelkey, S. M., et al. (2007), CRISM multispectral summary products: Parameterizing mineral diversity on Mars from reflectance, *J. Geophys. Res.*, *112*, E08S14, doi:10.1029/2006JE002831.

Petit, S. J., A. Decarreau, and F. Martin (1999), Characterization of octahedral substitutions in kaolinites using near infrared spectroscopy, *Clays Clay Miner.*, *47*, 103–108, doi:10.1346/CCMN.1999.0470111.

Post, J. L., and L. Borer (2000), High-resolution infrared spectra, physical properties, and micromorphology of serpentines, *Appl. Clay Sci.*, *16*, 73–85, doi:10.1016/S0169-1317(99)00047-2.

Post, J. L., and C. C. Plummer (1972), The chlorite series of Flagstaff Hill area, California: A preliminary investigation, *Clays Clay Miner.*, *20*, 271–283, doi:10.1346/CCMN.1972.0200504.

Poulet, F., et al. (2005), Phyllosilicates on Mars and implications for early Martian climate, *Nature*, *438*, 623–627, doi:10.1038/nature04274.

Poulet, F., et al. (2007), Martian surface mineralogy from Observatoire pour la Mineralogie, l'Eau, les Glaces et l'Activite on board the Mars Express spacecraft (OMEGA/MEx): Global mineral maps, *J. Geophys. Res.*, *112*, E08S02, doi:10.1029/2006JE002840.

Poulet, F., et al. (2008), Abundance of minerals in the phyllosilicate-rich units on Mars, *Astron. Astrophys.*, *487*, L41–L44, doi:10.1051/0004-6361:200810150.

Price, J. R., et al. (2005), Rates and time scales of clay-mineral formation by weathering in saprolitic regoliths of the southern Appalachians from geochemical mass balance, *Geol. Soc. Am. Bull.*, *117*(5–6), 783–794, doi:10.1130/B25547.1.

Rathbun, J. A., and S. W. Squyres (2002), Hydrothermal systems associated with Martian impact craters, *Icarus*, *157*, 362–372, doi:10.1006/icar.2002.6838.

Robert, C., and B. Goffe (1993), Zeolitisation of basalts in subaqueous freshwater settings: Field observations and experimental studies, *Geochim. Cosmochim. Acta*, *57*, 3597–3612, doi:10.1016/0016-7037(93)90142-J.

Robinson, D., and R. E. Bevins (1999), Patterns of regional low-grade metamorphism in metabasites, in *Low-Grade Metamorphism*, edited by M. Frey and D. Robinson, pp. 143–168, Blackwell Sci., Oxford, U. K.

Rosenberg, P. E. (2002), The nature, formation, and stability of end-member illite: A hypothesis, *Am. Mineral.*, *87*, 103–107.

Ruff, S. W. (2004), Spectral evidence for zeolite in the dust on Mars, *Icarus*, *168*, 131–143, doi:10.1016/j.icarus.2003.11.003.

Schiffman, P., and H. W. Day (1999), Petrological methods for the study of very low grade metabasites, in *Low-Grade Metamorphism*, edited by M. Frey and D. Robinson, pp. 108–142, Blackwell Sci., Oxford, U. K.

Schwenzer, S. P., and D. A. Kring (2009), Impact-generated hydrothermal alteration on Mars: Clay minerals, oxides, zeolites, and more, *Lunar Planet. Sci.*, *XL*, Abstract 1421.

Sheppard, R. A., and R. L. Hay (2001), Formation of zeolites in open hydrologic systems, in *Natural Zeolites: Occurrence, Properties, Applications*, edited by D. L. Bish and D. W. Ming, pp. 261–275, Mineral. Soc. of Am., Washington, D. C.

Squyres, S. W., et al. (2004), In-situ evidence for an ancient aqueous environment at Meridiani Planum, *Science*, *306*, 1709–1714, doi:10.1126/science.1104559.

Stolper, E. (1982), Water in silicate glasses: An infrared spectroscopic study, *Contrib. Mineral. Petrol.*, *81*, 1–17, doi:10.1007/BF00371154.

Swayze, G. A., et al. (2002), Mineral mapping Mauna Kea and Mauna Loa shield volcanoes on Hawaii using AVIRIS data and the USGS Tetracorder spectral identification system: Lessons applicable to the search for relict Martian hydrothermal systems, *JPL Publ.*, *03–4*, 373–387.

Swayze, G. A., R. N. Clark, A. F. H. Goetz, T. G. Chrien, and N. S. Gorelick (2003), Effects of spectrometer band pass, sampling, and signal-to-noise ratio on spectral identification using the Tetracorder algorithm, *J. Geophys. Res.*, *108*(E9), 5105, doi:10.1029/2002JE001975.

Swayze, G. A., et al. (2007), Spectral evidence for hydrated volcanic and/or impact glass on Mars with MRO CRISM, in *Seventh International Conference on Mars, July 9–13, 2007, Pasadena CA* [CD-ROM], *LPI Contrib.*, *1353*, Abstract 1353.

Tornabene, L. L., J. E. Moersch, H. Y. McSween Jr., V. E. Hamilton, J. L. Piatek, and P. R. Christensen (2008), Surface and crater-exposed lithologic units of the Isidis basin as mapped by co-analysis of THEMIS and TES derived data products, *J. Geophys. Res.*, *113*, E10001, doi:10.1029/2007JE002988.

Werner, S. C. (2005), Major aspects of the chronostratigraphy and geologic evolutionary history of Mars, Ph.D. thesis, Free Univ. of Berlin, Berlin.

Wichman, R. W., and P. H. Schultz (1989), Sequence and mechanisms of deformation around the Hellas and Isidis impact basins on Mars, *J. Geophys. Res.*, *94*, 17,333–17,357, doi:10.1029/JB094iB12p17333.

Weisenberger, T., and R. S. Selbekk (2008), Multi-stage zeolite facies mineralization in the Hvalfjordur area, Iceland, *Int. J. Earth Sci.*, *98*, 985–999, doi:10.1007/s00531-007-0296-6.

Wray, J. J., B. L. Ehlmann, S. W. Squyres, J. F. Mustard, and R. L. Kirk (2008), Compositional stratigraphy of clay-bearing layered deposits at Mawrth Vallis, Mars, *Geophys. Res. Lett.*, *35*, L12202, doi:10.1029/2008GL034385.

Ziegler, K., et al. (2003), Halloysite as a kinetically controlled end product of arid-zone basalt weathering, *Chem. Geol.*, *202*, 461–478, doi:10.1016/j.chemgeo.2002.06.001.

Zotov, A., et al. (1998), An experimental study of kaolinite and dickite relative stability at 150–300 degrees C and the thermodynamic properties of dickite, *Am. Mineral.*, *83*, 516–524.

O. Barnouin-Jha and S. L. Murchie, Johns Hopkins University Applied Physics Laboratory, Laurel, MD 20723, USA.

J. L. Bishop and D. J. Des Marais, NASA Ames Research Center, Mountain View, CA 94035, USA.

R. N. Clark and G. A. Swayze, U.S. Geological Survey, Box 25046, Denver, CO 80225, USA.

B. L. Ehlmann, J. F. Mustard, and L. H. Roach, Department of Geological Sciences, Brown University, Providence, RI 02912, USA.

R. E. Milliken, Jet Propulsion Laboratory, California Institute of Technology, Pasadena, CA 91109, USA.

F. Poulet, Institut d'Astrophysique Spatiale, Université Paris Sud, CNRS, F-91405 Orsay, France.

J. J. Wray, Department of Astronomy, Cornell University, Ithaca, NY 14853, USA.